A Unit Cell Model of a Regenerative Hydrogen-Vanadium Fuel Cell

C. A. Pino Muñoz,*,z H. Hewa Dewage, [a] V. Yufit, and N. P. Brandon**

Department of Earth Science and Engineering, Imperial College London, London SW7 2AZ, United Kingdom

In this study, a time dependent model for a regenerative hydrogen-vanadium fuel cell is introduced. This lumped isothermal model is based on mass conservation and electrochemical kinetics, and it simulates the cell working potential considering the major ohmic resistances, a complete Butler–Volmer kinetics for the cathode overpotential and a Tafel–Volmer kinetics near mass-transport free conditions for the anode overpotential. Comparison of model simulations against experimental data was performed by using a 25 cm^2 lab scale prototype operated in galvanostatic mode at different current density values ($50 - 600\ A\ m^{-2}$). A complete Nernst equation derived from thermodynamic principles was fitted to open circuit potential data, enabling a global activity coefficient to be estimated. The model prediction of the cell potential of one single charge-discharge cycle at a current density of $400\ A\ m^{-2}$ was used to calibrate the model and a model validation was carried out against six additional data sets, which showed a reasonably good agreement between the model simulation of the cell potential and the experimental data with a Root Mean Square Error (RMSE) in the range of 0.3–6.1% and 1.3–8.8% for charge and discharge, respectively. The results for the evolution of species concentrations in the cathode and anode are presented for one data set. The proposed model permits study of the key factors that limit the performance of the system and is capable of converging to a meaningful solution relatively fast (s–min).

 [DOI: 10.1149/2.1431714jes]

Manuscript submitted September 29, 2017; revised manuscript received November 17, 2017. Published December 30, 2017. This was Paper 23 presented at the National Harbor, Maryland Meeting of the Society, October 1–5, 2017.

Redox flow batteries are considered to be an exceptional candidate for grid-scale energy storage. One attractive feature is their capability to decouple power and energy.[1–4] All-Vanadium Redox Flow Batteries (VRFBs) have been considered a promising system due to the limited impact of cross-contamination. However, they have faced challenges related to cost, scale-up and optimization. Current research is also focused on improvement of electrolyte stability for use over a wider temperature window and concentrations, development of electrode materials resistant to overcharge, and mitigation of membrane degradation.[1,2] Cost dependency with regarding to vanadium can be mitigated through utilization of new systems that employ only half of the vanadium.[1] Recently, a Regenerative Hydrogen-Vanadium Fuel Cell (RHVFC) based on an aqueous vanadium electrolyte V(V) and V(IV) and hydrogen has been introduced[5] and is illustrated schematically in Figure 1. This system contains a porous carbon layer for the positive electrode reaction, membrane and catalyzed porous carbon layer for the negative electrode reaction. Hydrogen evolution, which is an adverse reaction in VRFBs, is here the main anodic process. During discharge, V(V) is reduced to V(IV) and H_2 is oxidized, while the reverse process occurs during charge and H_2 is stored. The vanadium reaction takes place in the positive electrode (cathode), while the hydrogen reaction occurs in the catalyst layer (CL) of the negative electrode (anode). The redox reactions that occur at the electrodes are presented in Equations 2 and 1, and the overall cell reaction in Equation 3, where the charged species VO^{2+} and VO_2^+ represent the V(IV) and V(V) oxidation states, respectively; and E° is standard potential with the subscripts ca and an referring to positive and negative side respectively.

$$2VO_2^+ + 4H_3O^+ + 2e^- \underset{\text{charge}}{\overset{\text{discharge}}{\rightleftharpoons}} 2VO^{2+} + 6H_2O, \qquad E^\circ_{ca} = 0.99\,V \qquad [1]$$

$$H_2 + 2H_2O \underset{\text{charge}}{\overset{\text{discharge}}{\rightleftharpoons}} 2H_3O^+ + 2e^-, \quad E^\circ_{an} = 0\,V \qquad [2]$$

$$2VO_2^+ + 2H_3O^+ + H_2 \underset{\text{charge}}{\overset{\text{discharge}}{\rightleftharpoons}} 2VO^{2+} + 4H_2O, \qquad E^\circ_{cell} = 0.99\,V \qquad [3]$$

The RHVFC could offer a better energy storage solution because of its fast hydrogen kinetics and absence of cross-mixing: even when the crossover of catholyte is possible, this could be collected at the anode side and pumped back to the catholyte tank.[5–7] An in depth analysis of the system by means of experimental studies has been reported previously by our group.[5,7] Yufit et al.[5] studied the performance of a RHVFC and observed that higher current densities or lower catholyte flow rates produce lower coulombic efficiencies, which can be explained by the mass transport limitations. Hewa Dewage et al.[7] studied the loss mechanisms of a RHVFC, observing crossover of vanadium, which could be adsorbed onto the anode Pt catalyst, and a negligible influence of the hydrogen flow rate. A better performance could be obtained if improved component materials and operating conditions were used. Modelling and simulation is an indispensable tool, saving time and reducing cost. To the best of the authors' knowledge, only one RHVFC model has been developed, as part of a PhD project,[8] which presented a one-dimensional steady-state approach. Common VRFB assumptions were considered for the cathode,[8–10] while the Membrane Electrolyte Assembly (MEA) was modeled using the assumptions developed by Bernardi and Verbrugge.[11,12] Only protons were allowed to cross the membrane, which was assumed

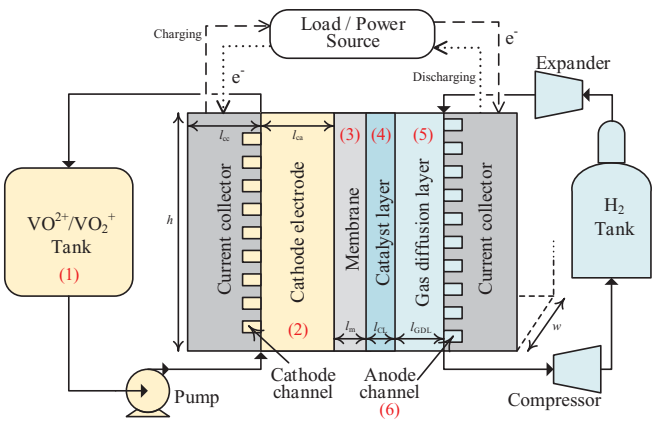

Figure 1. Schematic of the RHVFC and model domains.

*Electrochemical Society Student Member.
**Electrochemical Society Member.
[a]Present address: M-KOPA SOLAR Kenya Ltd.
[z]E-mail: c.pino15@imperial.ac.uk

to be fully hydrated since the catholyte is circulating through the cathode that is in direct contact with the membrane.[8] A similar assumption was made in a H_2/Br_2 battery model recently introduced by You et al.,[13] but the fully hydrated assumption was only considered at the membrane–cathode interface.

Detailed transport phenomena models have been developed for VRFBs and Polymer–Electrolyte–Membrane Fuel Cells (PEMFC).[14–18] Membrane water transport in PEMFC has been addressed following two mechanisms:[14,16,19] diffusive[20] and hydraulic.[11,12] The diffusive approach has been the preferred one since it describes more accurately non-flooded membranes.[16] Phase change processes such as membrane adsorption/desorption[21–24] and condensation/evaporation[22,24–27] have been also considered in PEMFC models.[16,19] Condensation and evaporation have been formulated using a switch function, as well as with overall rate constants. These constants were selected by He et al.[25] to practically generate an instantaneous process while other works have used values from 1 to 10^4 s^{-1}.[16,19] Adsorption and desorption have been formulated considering the departure from the equilibrium water content and to be proportional to rate constants that depend on the water content and temperature.[16,19] VRFB models have addressed the crossover of water and ionic species to evaluate self-discharge processes.[28–32] It has been observed in VRFBs that vanadium moves across the membrane due to the concentration gradient, while migration enhances or decreases the crossover flux depending on the relative direction of the concentration and potential gradients.[33] The crossover flux of VO^{2+} has been seen to approach the diffusive flux at Open Circuit Potential (OCP) under large negative current densities, whereas it can reach the sum of migration and electro-osmotic fluxes at large positive current densities.[33] A model that explained the crossover of all ionic species in VRFBs has been recently reported,[30,31] which indicated that convection transport produces the major contribution to vanadium ions crossover. For a Br_2/H_2 cell, minimal crossover during OCP has been observed, along with a strong dependency of crossover of water and bromine species with current density and minimal crossover of hydrogen which does not contribute importantly to the self-discharge of the cell.[33,34] In general, it has been stated for redox flow batteries that lower crossover of water and ionic species occurs for thicker membranes and an increase in crossover takes place with higher current densities.[33,34] This indicates that the relative importance of migration and electro-osmotic fluxes over diffusion flux increases as both the membrane thickness and current density increase.

Electrochemical reaction kinetics in PEMFCs are not fully understood since the oxygen and hydrogen reactions can be represented by different reaction paths with more than one step.[16,35,36] A Butler-Volmer relation has been widely used to model the kinetics, which uses transfer coefficients with values of about 0.5 for both electrodes and neglects the dependency on proton concentration and activity.[14,16] This assumption corresponds to the electro-neutrality condition assumed in the polymer electrolyte,[14,16] providing that the proton concentration is equal to the concentration of fixed charge sites. However, it has been reported that a Butler-Volmer type of expression does not represent correctly the relation between current density and overpotential for the hydrogen reaction.[35–37] The Open Circuit Potential (OCP) has been considered to be dependent on the pressure of hydrogen, oxygen and liquid water.[14] In VRFBs, the impact of using the complete Nernst equation (Equation 4) to describe the OCP has been stated by Knehr and Kumbur[38] and used in different models.[9,30,39–41]

$$E_{OCP} = E^{\circ}_{cell} + \frac{RT}{F}\ln\left(\frac{c^{ca}_{VO_2^+}\, c^{an}_{V^{2+}}\, (c^{ca}_{H^+})^2}{c^{ca}_{VO^{2+}}\, c^{an}_{V^{3+}}} \times \frac{c^{ca}_{H^+}}{c^{an}_{H^+}}\right) \quad [4]$$

This equation assumes that the activity coefficient (γ) for all species is equivalent to one, and includes the effect of the cathode proton concentration and Donnan potential, which represents the potential jump at the electrolyte-membrane interfaces due to different proton concentrations in the anolyte and catholyte.[38] However, the inconsistency with thermodynamics of this equation has been stated by Pavelka et al.,[42] who have introduced a OCP equation for VRFBs derived based on thermodynamic principles (Equation 5).

$$E_{OCP} = E^{\circ}_{cell} + \frac{RT}{F}\ln\left(\frac{a^{ca}_{VO_2^+}\, a^{an}_{V^{2+}}\, (a^{ca}_{H^+})^2}{a^{ca}_{VO^{2+}}\, a^{an}_{V^{3+}}\, a^{ca}_{H_2O}} \times \frac{a^{an}_{H^+}}{a^{ca}_{H^+}}\right) \quad [5]$$

This new equation differs from the equation proposed by Knehr and Kumbur in the inclusion of the potential difference between catholyte and anolyte, which is the dialysis potential or potential across the entire membrane.[42–44] The relation proposed by Pavelka et al. underestimated the OCP data when unity activity coefficients are considered.[42] To improve the agreement non-ideal activity coefficients should be considered, which can be evaluated from experimental OCP data. The reaction kinetics of VRFBs is commonly modeled using the Butler-Volmer equation,[18] which neglects the effect of the concentration of protons in the positive side.[10,30,41,45] It has been recognized that when the transfer coefficients in the Butler-Volmer equation are equal to 0.5, the ability to fit polarization data can be limited.[30,41]

The incorporation of detailed models in monitoring tools or stack models is currently not feasible.[46] Lumped parameter models are suitable for these applications since they are typically based on a small set of differential algebraic equations, which can be fairly simple to integrate and can be accurate enough to describe the battery dynamics.[18] Lumped models consider the time dependent electrochemical phenomena, but assuming a uniform spatial distribution of species concentrations. A VRFB lumped model was developed by Shah et al.,[46] which considered mass conservation and the electrochemical processes, and could capture the relation between performance and key properties.[18] Additional effects were later included such as thermal processes,[47,48] self discharge,[29,49,50] pumping power and shunt current losses.[51,52] A PEMFC lumped model was developed by Pukrushpan et al.,[53] which allowed the evolution of component partial pressures and membrane humidity to be studied.[54] Effects such as reactant starvation and flooding were later considered to describe the effect of water accumulation on the cell behavior.[55,56]

In this paper, a simplified model for a unit cell of a hydrogen vanadium system is presented, which was based on the physicochemical phenomena explained by mass conservation, transport mechanisms and electrochemical processes, but maintaining simplicity to allow its use in monitoring and designing. The aim of this model is to provide a first approximation of interplay of various physicochemical phenomena involved in a RHVFC. It is hoped that this model will accelerate the advancement of the knowledge and quantification of the relevant physical and electrochemical processes, helping to distinguish the key phenomena. The paper presents a detailed explanation of the proposed comprehensive model, stating equations, assumptions, limitations and capabilities of the model to represent experimental data, as such it is expected to provide a baseline for more in-depth representations developed in future. In the following sections the model equations are presented followed by the experimental details and a discussion of the model calibration and validation.

Mathematical Model

The proposed mathematical model was developed considering six domains: (1) catholyte tank, (2) cathode, (3) membrane, (4) CL, (5) Gas Diffusion Layer (GDL), and (6) the anode channel, as shown in Figure 1. The cathode channel was not included as a domain since the flow rate through it was assumed to by-pass the porous electrode and to not participate in any reaction. The hydrogen tank was not considered in the model because the hydrogen flow is passed through the cell and not recirculated to a tank in the experimental set-up that was used (see Experimental section).

The model was developed based on the following assumptions and simplifications:

1. All domains are considered isothermal.
2. Electrolyte is considered incompressible, having constant density, viscosity and volume.

3. Physical properties and mass and charge transfer properties are assumed isotropic and homogeneous in all the domains.
4. The electrolytes must maintain electro-neutrality.
5. Unit activity coefficients are assumed for all species. However, an activity term is considered for the chemical dissociation of H_2SO_4, and a fitted global activity coefficient is considered for the estimation of OCP.
6. Dilute solution approximation is considered.
7. Spatial concentration distribution in the catholyte tank, cathode, CL and anode channel are neglected.
8. Membrane and GDL are considered to be steady-state.
9. Gas evolution reactions in the cathode are neglected.
10. Dissociation of bi-sulfate ions is assumed to reach equilibrium instantaneously.
11. Full humidification of the membrane is assumed at the cathode – membrane interface.
12. The ionomer phase that is present in the CL has the same fixed charge concentration as the ionomer in the membrane.
13. Protons are the only ionic species that can cross the membrane.
14. Water crossover from cathode to anode is considered, but any change of the catholyte volume is neglected.
15. Water only in vapor phase can leave the CL and enters the anode channel or vice-versa, and can leave the system.
16. The gas phase at the anode side is treated as an ideal gas.

Cathode and catholyte tank.—The catholyte has been considered to contain water, sulphuric acid species (H^+, HSO_4^- and SO_4^{2-}) and charged vanadium species (VO^{2+} and VO_2^+). A correct estimation of the initial concentration of ionic species in the catholyte is important to maintain electro-neutrality ($\sum z_i c_i = 0$), and to calculate the equilibrium potential (Equation 40) and overpotential (Equation 46). The H_2SO_4 dissociation is considered to follow a two-step processes, Equations 6 and 7, where k_1 and k_2 represent the first and second dissociation constants, respectively.

$$H_2SO_4 + H_2O \longrightarrow H_3O^+ + HSO_4^-, k_1(\text{strong acid}) \quad [6]$$

$$HSO_4^- + H_2O \longleftrightarrow H_3O^+ + SO_4^{2-}, k_2 \quad [7]$$

The first step of dissociation is assumed to be fully complete since it has been reported that it is essentially complete for concentrations up to 40 mol kg^{-1} at temperatures between 273 and 323 K.[57] In chemical equilibrium, the second step of dissociation, that noticeably depends on temperature, is described by the dissociation constant of bi-sulfate ion (k_2), which is defined by the activities (a_i) of the sulphuric acid species and can be related to their molar concentrations (c_i) and activity coefficients (γ_i) according to $a_i = \gamma_i c_i / c^\circ$, where the standard molarity c° is 1 mol L^{-1}.

$$k_2(T) = \frac{c_{H^+} c_{SO_4^{2-}}}{c_{HSO_4^-} c^\circ} \frac{\gamma_{H^+} \gamma_{SO_4^{2-}}}{\gamma_{HSO_4^-}} = Q_M(T)\gamma(T) \quad [8]$$

The derivation of Equation 8 is similar to the one presented by Knopf and co-workers,[57] but the reference concentration has been changed from molality to molarity, and includes a molar equilibrium dissociation quotient, $Q_M(T)$, and an activity coefficient product, $\gamma(T)$. The experimental molality data of H_2SO_4 dissociation presented in their work[57] was transformed to molarity and fitted to a simple empirical model. Figure 2 presents the values of Q_M at 290 K as a function of H_2SO_4 molar concentration and the proposed empirical model.

The conservation of mass for each ionic species in the cathode during charge and discharge is presented in Equations 9–13. These equations include the change in the concentration of species entering to the cathode due to the recirculation of the catholyte through the tank; the electron transfer reaction according to Equation 1; the dissociation of bi-sulfate ion according to Equation 7; and the transport of protons through the membrane. The term S_d^{eq} that represents the change in concentration of species due to the dissociation of bi-sulfate ions

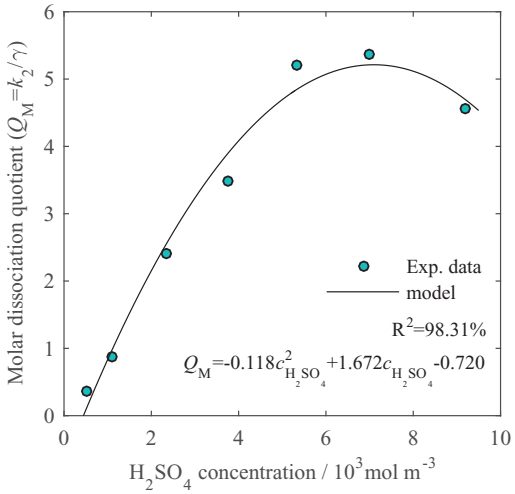

Figure 2. Dependency of Q_M with the molar concentration of H_2SO_4 at 290 K. Experimental data estimation based on experimental data presented by Knopf et al.[57]

(Equation 7) is obtained by means of Equation 8. Table I shows the input parameters used on the cathode side.

$$\varepsilon_{ca} V_{ca} \frac{dc_{VO^{2+}}}{dt} = Q_{ca}(c_{VO^{2+},T} - c_{VO^{2+}}) \mp \frac{A_{ca} j}{F} \quad [9]$$

$$\varepsilon_{ca} V_{ca} \frac{dc_{VO_2^+}}{dt} = Q_{ca}(c_{VO_2^+,T} - c_{VO_2^+}) \pm \frac{A_{ca} j}{F} \quad [10]$$

$$\varepsilon_{ca} V_{ca} \frac{dc_{H^+}}{dt} = Q_{ca}(c_{H^+,T} - c_{H^+}) \pm \frac{2A_{ca} j}{F} \mp \frac{A_{ca} j}{F} + S_d^{eq} \quad [11]$$

$$\varepsilon_{ca} V_{ca} \frac{dc_{SO_4^{2-}}}{dt} = Q_{ca}(c_{SO_4^{2-},T} - c_{SO_4^{2-}}) + S_d^{eq} \quad [12]$$

$$\varepsilon_{ca} V_{ca} \frac{dc_{HSO_4^-}}{dt} = Q_{ca}(c_{HSO_4^-,T} - c_{HSO_4^-}) - S_d^{eq} \quad [13]$$

The terms c_i and $c_{i,T}$ denote the bulk concentration of species i in the electrolyte at the cathode and catholyte tank, respectively. The symbol ε_k, V_k and A_k represent the porosity, volume and cross-sectional are of the domain k. The term t is time, Q_{ca} is the flow rate of catholyte in the cathode, j is the applied current density (current per unit of cross-sectional area of electrode), and F is the Faraday constant.

The mass conservation equations for all ionic species in the catholyte tank is given as follows:

$$V_T \frac{dc_{i,T}}{dt} = Q_{ca}(c_i - c_{i,T}), \quad i = \left[VO^{2+}, VO_2^+, H^+, SO_4^{2-}, HSO_4^-\right] \quad [14]$$

Where V_T is the catholyte tank volume.

The catholyte flow rate flows through the serpentine flow channel while penetrates into the porous electrode. A steady state condition was assumed to describe a simplified flow distribution inside of the positive half-cell,[59] i.e., $\Delta p_{ca} = \Delta p_{CH}$, allowing to calculate the flow rate in the channel and porous electrode. The catholyte flow rate that flows through the flow channels was assumed to by-pass the reaction area (porous electrode). According to Darcy's law, the pressure drop through the porous electrode (Δp_{ca}) can be calculated as,[59]

$$\Delta p_{ca} = \frac{\mu L_{ca} Q_{ca}}{\kappa A_{ca}} \quad [15]$$

Table I. Cathode side parameters.

Parameter	Symbol	Value	Unit	Source
Height of cathode	h_{ca}	0.05	m	Experimental setup[7]
Width of cathode	w_{ca}	0.05	m	Experimental setup[7]
Thickness of cathode	l_{ca}	0.0004	m	Experimental setup[7]
Porosity of cathode	ε_{ca}	0.88	—	Gandomi et al.[41]
Electronic conductivity of cathode	σ_{ca}	482.4	Sm^{-1}	Gandomi et al.[41]
Mean fiber diameter	d_f	17.6×10^{-6}	m	Gandomi et al.[41]
Specific surface area of the cathode	S_{ca}	2.7×10^{4}	$m^2\,m^{-3}$	Estimated[58] ($S_{ca} = 4(1-\varepsilon_{ca})/d_f$)
Nernst diffusion layer	δ_0	84.8×10^{-6}	m	Fitted
Volume of catholyte in tank	V_T	6×10^{-5}	m^3	Experimental setup[7]
VO^{2+} diffusion coefficient in the catholyte	$D_{VO^{2+}}$	3.9×10^{-10}	$m^2\,s^{-1}$	Gandomi et al.[41]
VO_2^+ diffusion coefficient in the catholyte	$D_{VO_2^+}$	3.9×10^{-10}	$m^2\,s^{-1}$	Gandomi et al.[41]
H^+ diffusion coefficient in the catholyte	D_{H^+}	9.3×10^{-9}	$m^2\,s^{-1}$	Gandomi et al.[41]
Catholyte density	ρ	1350	$kg\,m^{-3}$	Gandomi et al.[41]
Catholyte dynamic viscosity	μ	0.005	Pa s	Gandomi et al.[41]
Kozeny-Carman constant	K_{KC}	180	–	Gandomi et al.[41]

where the effective permeability of the cathode (κ) can be determined using Kozeny-Carman equation[30,59] as below,

$$\kappa = \frac{\varepsilon_{ca}^3 d_f^2}{K_{KC}(1-\varepsilon_{ca})^2} \quad [16]$$

In the above equations, μ is the dynamic viscosity of the catholyte, which was considered constant at its value for 50% State Of Charge (SOC).[30] L_{ca} is the cathode flow length, A_{ca} is the flow area of electrode, d_f is the mean fiber diameter of the electrode, and K_{KC} is the Kozeny-Carman constant.

The pressure drop through the channel can be calculated considering two sources: friction pressure drop and minor pressure drops, which are caused by sudden change in fluid direction or velocity.[59] Considering these two parts, the pressure drop through the channel (Δp_{CH}) can be obtained as,[59]

$$\Delta p_{CH} = \left(f_{CH} \frac{L_{CH}}{D_{h,CH}} + K_f \right) \frac{\rho}{2A_{CH}} Q_{CH}^2 \quad [17]$$

where the friction resistance coefficient (f_{CH}) can be obtained as shown below,

$$f_{CH} = \frac{56.91}{Re_{D_{h,CH}}}, \quad Re_{D_{h,CH}} = \frac{\rho D_{h,CH} Q_{CH}}{\mu A_{CH}} \quad [18]$$

The value 56.91 in Equation 18 is determined considering the specific geometry of the channel.[59,60] In the above equations, $D_{h,ch}$ is the hydraulic diameter of the channel ($D_{h,CH} = 4A_{CH}/P_{CH}$), K_f is the minor resistance coefficient, ρ is the density of the catholyte, A_{ch} is the area of the channel, Q_{ch} is the flow rate in the channel and Re_{D_h} is the Reynolds number based on the hydraulic diameter.

Anode catalyst layer.—The anode side was modeled considering the CL, GDL and anode channel. Figure 3 shows the molar flow rates ($\dot{n}_i$) that were considered in the mass conservation equations of the different species. In Figure 3, the direction of the arrows represent positive values for the mass transport of species through the membrane and GDL, reaction of hydrogen in the CL, desorption of liquid water in the CL, and phase change between vapor and liquid water in the CL and anode channel. At the CL, protons ($\dot{n}_{H^+,m}$) and dissolved water can arrive or leave due to transport through the membrane. Significant self-discharge of redox flow batteries due to crossover of ionic species has been observed,[33,34] which increases with current density. Crossover fluxes of VO^{2+} and VO_2^+ through the membrane have been neglected in this model (Assumption 13), but will be incorporated in future work. The dissolved water is transported by electro-osmotic drag ($\dot{n}_{EO}$) and diffusion ($\dot{n}_{diff}$), which was considered to always be in the direction of the CL because of Assumption 11. The dissolved water in the CL can be desorbed ($\dot{n}_{des}$) into liquid water, which can receive or lose material by evaporation/condensation ($\dot{n}_{wv,CL}$) depending on the vapor pressure and its saturation pressure. Hydrogen/protons are oxidized/reduced by means of the electron-transfer reaction ($\dot{n}_{H_2,react}$) and hydrogen can be transported from the CL through the GDL into the channel or vice-versa, along with water vapor ($\dot{n}_{H_2,GDL}$ and $\dot{n}_{v,GDL}$). In the channel, pure hydrogen is entering ($\dot{n}_{H_2,IN}$), the phase change between vapor and liquid is considered ($\dot{n}_{wv,CH}$), and the outlet only contains hydrogen and water vapor ($\dot{n}_{H_2,OUT}$ and $\dot{n}_{v,OUT}$).

The mass conservation equation for each species during charge and discharge in the CL is presented in Equations 19–23.Table II shows the parameter values for the anode side. The concentration of protons (Equation 19) is presented as steady-state because of Assumption 4, which is $c_{H^+} + z_f c_f = 0$ where z_f and c_f are the charge number and concentration of the fixed charge in the electrolyte. The balance of hydrogen and water vapor includes the transport through the GDL, which is explained in the following Gas diffusion layer subsection.

$$V_{CL}\varepsilon_m \frac{dc_{H^+}}{dt} = \dot{n}_{H^+,m} \mp \frac{A_{CL} j}{F} = 0 \quad [19]$$

$$V_{CL}\varepsilon_{CL}(1-s_{CL})\frac{dc_{H_2,CL}}{dt} = \pm\frac{A_{CL} j}{2F} - \dot{n}_{H_2,GDL} \quad [20]$$

In the above equations, V_{CL} is the CL volume, ε_m is the volume fraction of electrolyte membrane in the CL, A_{CL} is the cross-sectional

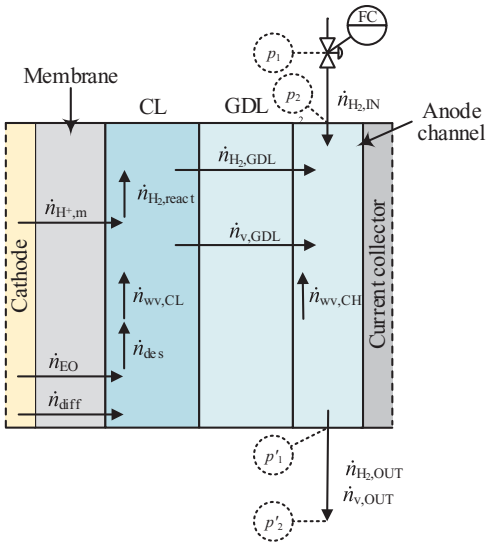

Figure 3. Schematic of molar flow rates at anode side.

Table II. Anode side parameters.

Parameter	Symbol	Value	Unit	Source
Height of anode	h_{an}	0.05	m	Experimental setup[7]
Width of anode	w_{an}	0.05	m	Experimental setup[7]
Thickness of CL	l_{CL}	1×10^{-5}	m	Estimated as 10% of l_{an}
Thickness of GDL	l_{GDL}	1.9×10^{-4}	m	Estimated as 90% of l_{an}
Porosity of CL	ε_{CL}	0.3	—	Wu et al.[24]
Mean pore size in GDL	d_p	1×10^{-5}	m	Estimated
Porosity of GDL	ε_{GDL}	0.6	—	Wu et al.[24]
Electronic conductivity of CL	σ_{CL}	114	S m^{-1}	Wu et al.[62]
Electronic conductivity of GDL	σ_{GDL}	114	S m^{-1}	Wu et al.[62]
Roughness factor of CL	R_{an}	200	m^2 m^{-2}	Estimated[63]
Volume fraction of polymer electrolyte in CL	ε_m	0.3	—	Wu et al.[24]

area of the CL, ε_{CL} is the porosity of the CL ans s_{CL} is the liquid saturation in the CL.

Water was considered to exist in three different phases depending on the domain,[24,27] i.e., water vapor (v), liquid water (w) and dissolved water (dw). The transport of water through the polymer electrolyte is assumed to happen in the dissolved phase since the pore size of the polymer electrolyte is of the order of only 10 nm and clusters of water tend to be localized and less connected.[24] The mass conservation for the water species in the CL are given as follows:

$$V_{CL}\varepsilon_m\frac{dc_{dw}}{dt} = -V_{CL}\varepsilon_m\gamma_{des}(c_{dw,CL} - c_{dw}^{eq}) + \xi_{drag}\frac{A_{CL}j}{F} - A_m D_{dw,m}\frac{(c_{dw,CL} - c_{dw,c-m})}{l_m} \quad [21]$$

$$V_{CL}\varepsilon_{CL}\frac{\rho_w}{M_w}\frac{ds_{CL}}{dt} = V_{CL}\varepsilon_m\gamma_{des}(c_{dw,CL} - c_{dw}^{eq}) + R_{w,CL} \quad [22]$$

$$V_{CL}\varepsilon_{CL}(1 - s_{CL})\frac{dc_{v,CL}}{dt} = -R_{w,CL} - \dot{n}_{v,GDL} \quad [23]$$

Where γ_{des} is the desorption rate, ξ_{drag} is the electro-osmotic drag coefficient, $D_{dw,m}$ is the diffusion coefficient of dissolved water in the electrolyte membrane, l_m is the thickness of the membrane, ρ_w is the water density, M_w is the molar weight of water and $R_{w,CL}$ is the term that represents the phase change between vapor and liquid water in the CL.

A diffusive approach was considered for the transport of dissolved water through the membrane, Equation 21, accounting for electro-osmotic drag with $\xi_{drag} = 2.5\lambda/22$,[20] diffusion transport and a desorption term. The diffusion coefficient of dissolved water is given by Equation 24. The desorption was assumed to be proportional to the difference between the actual electrolyte membrane water content, λ (Equation 25), and the equilibrium water content, λ^{eq} (Equation 26), which was determined by experimental results of water uptake in CLs.[61] The desorption rate was defined by an empirical relationship that depends on the local electrolyte membrane hydration,[24] Equation 27.

$$D_{dw,m} = 4.1 \times 10^{-10}\left(\frac{\lambda}{25}\right)^{0.15}\left[1 + \tanh\left(\frac{\lambda - 2.5}{1.4}\right)\right] \quad [24]$$

$$c_{dw} = \lambda\frac{\rho_{dm}}{EW} \quad [25]$$

$$\lambda_{CL}^{eq} = 0.0514 + 10.987a_v - 13.164a_v^2 + 5.777a_v^3 \quad [26]$$

$$\gamma_{des} = \frac{4.59 \times 10^{-5} f_V}{l_{CL}}\exp\left[2416\left(\frac{1}{303} - \frac{1}{T}\right)\right], \quad f_V = \frac{\lambda V_w}{V_m + \lambda V_w} \quad [27]$$

In the above equation, ρ_{dm} is the dry membrane density, EW is the equivalent molecular weight of the dry membrane, a_i is the activity of species i, f_V is the volume fraction of water in the membrane, V_w water molar volume, V_m is the dry membrane molar volume, l_{CL} is the thickness of the CL, and T is the temperature. V_m can be calculated by $V_m = EW/\rho_m$.[21]

The phase change between liquid and vapor for the water is presented in a switching format, Equation 28. Where k_c and k_e are the condensation and evaporation rate constants, y_v is the molar fraction of vapor in the gas phase, p_v is the vapor pressure and p_v^{sat} is the saturation pressure. The mass-transfer rate is related to the amount of reactant in the porous media and the driving force,[25] which is the difference between the vapor pressure and its saturation pressure. The restriction that when no liquid water is present and the vapor pressure is lower than the saturation pressure, Equation 28 is not valid and no evaporation can occur, must be included.

$$R_w = \begin{cases} k_c V\varepsilon(1-s)y_v\frac{(p_v - p_v^{sat})}{RT}, & \text{if } p_v \geq p_v^{sat}(\text{cond.}) \\ k_e V\varepsilon s\frac{\rho_w}{M_w}(p_v - p_v^{sat}), & \text{if } p_v < p_v^{sat}(\text{evap.}) \end{cases} \quad [28]$$

Gas diffusion layer.—The Dusty Gas Model (DGM), which considers both diffusion and pressure-driven convection,[64] was used to model transport through the GDL and only the steady-state transport of hydrogen and water vapor was modeled. Equation 29 was used to describe the transport of a binary mixture[65] (H_2 and water vapor (v)), accounting for the difference of molar fraction and pressure. The molar flow rate of species can be obtained by means of the following relation, $\dot{n}_{i,GDL} = A_{GDL}N_{i,GDL}$, where A_{GDL} is the cross-sectional area of the GDL and N_i is the molar flux of species i. The effective binary diffusion coefficient ($D_{i,j}^{eff}$) was estimated from Chapman-Enskog kinetic theory assuming ideal gas behavior holds[66] (Assumption 16) and is given in equation 30. The effective Knudsen diffusion coefficient ($D_{Kn,i}^{eff}$) and permeability of the porous material (K) were calculated using Equation 31.[65]

$$N_i = -\frac{p}{RT}\alpha_i^{-1}\nabla y_i - \frac{y_i}{RT}\left(\alpha_i^{-1}\left(1 + \frac{D_{Kn,j}^{eff}}{D_{i,j}^{eff}}\right) + \frac{Kp}{\mu}\right)\nabla p$$

$$\alpha_i = \frac{1}{D_{Kn,i}^{eff}} + \frac{y_j}{D_{i,j}^{eff}}\left(1 + \frac{y_i}{y_j}\left(\frac{M_i}{M_j}\right)^{0.5}\right), \quad i, j = H_2, v \quad [29]$$

$$D_{i,j}^{eff} = \frac{\varepsilon}{\tau}1.858 \times 10^{-7}T^{3/2}\frac{[(M_i + M_j)/M_iM_j]^{0.5}}{p\sigma_{ij}^2\Omega_D} \quad [30]$$

$$D_{Kn,i}^{eff} = \frac{\varepsilon}{\tau}\frac{1}{3}d_p\left(\frac{8RT}{\pi M_i}\right)^{0.5}, \quad K = \frac{\varepsilon}{\tau}\frac{d_p^2}{32} \quad [31]$$

Both diffusion coefficients were corrected considering porosity and tortuosity (τ) of the porous media using a Bruggeman correlation,[19,67]

Table III. Electrochemical and transport parameters.

Parameter	Symbol	Value	Unit	Source
Condensation rate constant	k_c	100	s^{-1}	He et al.[25]
Evaporation rate constant	k_e	100	$atm^{-1}\ s^{-1}$	He et al.[25]
Molecular radius of hydrogen	σ_{H_2}	2.827	Å	Reid et al.[68]
Molecular radius of vapor	σ_v	2.641	Å	Reid et al.[68]
Lennard-Jones potential of hydrogen	ϵ_{H_2}/k	59.7	K	Reid et al.[68]
Lennard-Jones potential of vapor	ϵ_v/k	809.1	K	Reid et al.[68]
Standard reaction rate constant for cathode	$k_{ca,ref}$	1.2×10^{-7}	$m\ s^{-1}$	Fitted
Transfer coefficient for vanadium reaction	α	0.55	—	Knehr et al.[30]
Parameter as defined in Equation 54	$Z^{\oslash}$	0.42	—	Kucernak & Zalitis[35]
Parameter as defined in Equation 54	$B^{\oslash}$	0.28	—	Kucernak & Zalitis[35]
Desorption rate constant	$k^{\oslash}_{des}$	2.1×10^{-5}	$mol\ cm^{-2}s^{-1}$	Kucernak & Zalitis[35]
Activation energy of hydrogen reaction	E_a	2.3×10^4	$kJ\ mol^{-1}$	Kucernak & Zalitis[35]
Transfer coefficient for hydrogen reaction	β	0.52	—	Kucernak & Zalitis[35]

$\tau = \varepsilon^{-1/2}$. The effect of liquid saturation over the transport parameters was neglected because of Assumption 15, which results in no liquid water in the GDL. In the above equations, R is the universal gas constant, K is the permeability, μ is the gas dynamic viscosity, M_i is the molecular weight of species i, σ_{ij} is the characteristic binary Lennard-Jones length, Ω_D is the diffusion collision integral, and d_p is the mean pore size. The parameters σ_{ij} and Ω_D are given by Equations 32 and 33, where σ_i and ϵ_i are the characteristic Lennard-Jones energy and length, ϵ_{ij} is the characteristic binary Lennard-Jones energy, and k_B is the Boltzmann constant. Table III presents the electrochemical and transport parameters that were considered in the model.

$$\sigma_{ij} = \frac{(\sigma_i + \sigma_j)}{2} \quad [32]$$

$$\Omega_D = \frac{1.06036}{(T^*)^{0.15610}} + \frac{0.19300}{\exp(0.47635T^*)} + \frac{1.03587}{\exp(1.52996T^*)} + \frac{1.76474}{\exp(3.89411T^*)} \quad [33]$$

where,

$$T^* = k_B T/\epsilon_{ij}, \quad \epsilon_{ij} = (\epsilon_i \epsilon_j)^{1/2} \quad [34]$$

Anode channel.—At the inlet, dry hydrogen is entering, and at the outlet, hydrogen and water vapor leave the anode channel. Liquid water was not considered to leave the channel (Assumption 15). The mass conservation equations of hydrogen, vapor water and liquid water are given in Equations 35, 36 and 37, respectively. Inside the anode channel the phase change between vapor and liquid water is given by Equation 28. The mass flux (G) that enters and leaves the anode channel was estimated through an isothermal energy balance,[69] Equation 38, considering the fanning friction factor (f_F) for laminar flow, $f_F = 16/Re$, where Re is the Reynolds number. Figure 3 shows the two positions considered in each energy balance in the inlet (p_1 and p_2) and outlet (p_1' and p_2'). After solving Equation 38 assuming laminar flow at the inlet and outlet, the Reynolds number was recalculated and a value around 4.5 was obtained for inlet and outlet, which fulfills the previous assumption (i.e., $Re < 2000$).

$$V_{CH}(1 - s_{CH})\frac{dc_{H_2,CH}}{dt} = \dot{n}_{H_2,GDL} + \dot{n}_{H_2,IN} - \dot{n}_{H_2,OUT} \quad [35]$$

$$V_{CH}(1 - s_{CH})\frac{dc_{v,CH}}{dt} = -R_{w,CH} + \dot{n}_{v,GDL} - \dot{n}_{v,OUT} \quad [36]$$

$$V_{CH}\frac{\rho_w}{M_w}\frac{ds_{CH}}{dt} = R_{w,CH} \quad [37]$$

$$G^2 = \frac{M}{RT}\frac{d}{4f_F L}(p_1^2 - p_2^2),\ Re = \frac{\rho v_m d}{\mu} \quad [38]$$

In the above equations, V_{CH} is the anode channel volume, s_{CH} is the liquid saturation in the anode channel, $R_{w,CH}$ is the term that represents the phase change between vapor and liquid water in the anode channel, M is the molecular weight of the gas, d is the pipe diameter, L is the pipe length, p_1 and p_2 are the pressure and the initial and final point, ρ is the gas density, and v_m is the mean velocity of the fluid.

Cell potential.—The operating cell potential, E_{cell} was estimated considering the reversible OCP (E_{OCP}), ohmic overpotential (η_{ohm}) and electrode overpotentials (η_{ca}) and (η_{an}),[70] Equation 39. Where the overpotentials are added to E_{OCP} for charge operation and are subtracted for discharge operation.

$$E_{cell} = E_{OCP} \pm \eta_{ohm} \pm |\eta_{ca}| \pm |\eta_{an}| \quad [39]$$

A complete Nernst equation to estimate the OCP was derived form thermodynamics as explained in Appendix A. Considering Equation A12 and assuming the activity of water ($a^{ca}_{H_2O}$) in the catholyte equal to 1 and Henry's law for hydrogen, which considers the activity of dissolved hydrogen equivalent to the change in partial pressure of hydrogen.[35] The OCP can be expressed as,

$$E_{OCP} = E^{\circ}_{cell} + \frac{RT}{F}\ln\left(\frac{c^{ca}_{VO_2^+} c^{ca}_{H^+} (p^g_{H_2})^{0.5}}{c^{ca}_{VO^{2+}}} \times \frac{\gamma^{ca}_{VO_2^+}\gamma^{ca}_{H^+}}{\gamma^{ca}_{VO^{2+}}}\right) \quad [40]$$

To further simplify Equation 40 and considering the difficulty in obtaining data of activity coefficients, a global activity term was considered ($\gamma_{OCP} = \gamma^{ca}_{VO_2^+}\gamma^{ca}_{H^+}/\gamma^{ca}_{VO^{2+}}$). Equation 40 considers the potential difference of the catholyte and anolyte at equilibrium, which was obtained by the condition of equality of electrochemical potential of protons in the catholyte and anolyte,[42–44] see Appendix A. An equivalent expression for OCP can be derived, if the Nernst equation is considered along with the potential jump (Donnan potential) that appears at the two membrane – electrolyte interfaces due to the difference in concentration of protons.[42] This potential across the entire membrane, namely dialysis potential, derived from thermodynamics differs from the relation presented by Knehr and Kumbur[38] as has been stated by Pavelka et al.[42]

The ohmic overpotential was calculated by adding the contribution of the different domain: current collectors (cc), catholyte (ca-el), cathode (ca), membrane (m), CL, polymer electrolyte in the CL (CL-m) and GDL; and were described by means of Ohm's law,[46,72] as shown in Equations 41 and 42. In addition, an extra ohmic resistance (R_C) was included to account for any additional resistance, such as the contact resistance between current collectors and porous electrodes[10,73] and changes in the membrane conductivity due to uptake of ionic

Table IV. Properties of membrane and current collectors.

Parameter	Symbol	Value	Unit	Source
Height of membrane	h_m	0.05	m	Experimental setup[7]
Width of membrane	w_m	0.05	m	Experimental setup[7]
Total cross-sectional area of current collectors	A_{cc}	0.0073	m^2	Experimental setup[7]
Thickness of membrane	l_m	1.83×10^{-4}	m	Supplied by manufacturer[71]
Thickness of current collectors	l_{cc}	0.005	m	Experimental setup[7]
Electronic conductivity of current collectors	σ_{cc}	1000	$S\,m^{-1}$	Knehr et al.[30]
Extra ohmic resistance	R_C	0.3/3.6	$\Omega\,cm^2$	Fitted
Dry membrane density	ρ_m	2000	$kg\,m^{-3}$	Ge et al.[21]
Equivalent weight of polymer electrolyte	EW	1.1	$kg\,mol^{-1}$	Ge et al.[21]
Molar volume of water	V_w	1.8×10^{-5}	$m^3 mol^{-1}$	Ge et al.[21]
Fixed acid concentration	c_f	1200	$mol\,m^{-3}$	Ge et al.[21]
Fixed acid charge	z_f	-1	—	—

species.[74]

$$\eta_{ohm}^{cc} = j\frac{l_{cc}}{\sigma_{cc}}, \quad \eta_{ohm}^{m} = j\frac{l_m}{\sigma_m}, \quad \eta_{ohm}^{C} = jR_C \qquad [41]$$

$$\eta_{ohm}^{k} = j\frac{l_k}{\sigma_k^{eff}}, \quad k = [ca-el, ca, CL, CL-m, GDL] \qquad [42]$$

Where l_k and σ_k are the thickness and conductivity of the domain k, and the superscript 'eff' denotes an effective property. Table IV shows the property values for the membrane and current collectors.

The Nafion membrane conductivity was described as a function of the water content (λ) and temperature through an empirical relation presented in Equation 43.[20,72]

$$\sigma_m = (0.5139\lambda - 0.326)\exp\left(1268\left[\frac{1}{303} - \frac{1}{T}\right]\right) \qquad [43]$$

The effect of the membrane uptake of sulphuric acid and vanadyl on membrane conductivity has been studied by Tang et al.,[74] who observed an enhancement or reduction of membrane conductivity depending on acid and water content in the membrane. An increase in the concentration of protons due to acid presence in the membrane can enhance conductivity, while mobility of protons significantly decreases with water loss.[74] When a nafion membrane was equilibrated with a electrolyte solution of practical composition for VRFB operation, uptake of vanadyl and acid contributes to reduce membrane conductivity to some extent, and a complicated equilibrium and partitioning competition between protons and vanadyl has been suggested.[74] Future studies should focus on the membrane-electrolyte equilibrium in the RHVFC to assess membrane conductivity, concentration and mobility of protons by means of a detailed transport model of water and ionic species through the membrane.

The electrolyte conductivity was estimated considering the concentration and charge of all ionic species in the electrolyte,[45] Equation 44. A Bruggemann correction was applied to account for the porous electrode,[45] allowing for the calculation of the effective conductivity of electrolytes and electrodes as shown in Equation 45.

$$\sigma_{ca-el} = \frac{F^2}{RT}\sum_i z_i^2 D_{i,el} c_i, \quad i = \left[VO^{2+}, VO_2^+, H^+, SO_4^{2-}, HSO_4^-\right] \qquad [44]$$

$$\sigma_{ca-el}^{eff} = \varepsilon_{ca}^{3/2}\sigma_{ca-el}, \quad \sigma_{ca}^{eff} = (1-\varepsilon_{ca})^{3/2}\sigma_{ca}, \quad \sigma_{CL}^{eff} = (1-\varepsilon_{CL}-\varepsilon_m)^{3/2}\sigma_{CL}, \quad \sigma_{CL-m}^{eff} = \varepsilon_m^{3/2}\sigma_{CL-m} \qquad [45]$$

In the above equations, z_i is the charge number of species i and $D_{i,el}$ is the diffusion coefficient of species i in the electrolyte.

The electrode overpotential with contribution of cathode and anode was considered to estimate the cell potential. The cathode overpotential (η_{ca}) was calculated by a Butler–Volmer (BV) kinetic approach[45,46] (Equation 46), where all the ionic species involved in the redox reaction were considered.[75,76] This expression does not consider activity coefficients for the ionic species, because of the difficulty in estimating individual activity coefficients or decoupling their values from the fitted global activity terms (γ_{OCP}). It is expected that the fitting parameters used in the Butler-Volmer equation absorb to some extend the effect of neglecting the activity coefficients.

$$j^{BV} = j_{0,ca}^{BV}\left(\left[\frac{c_{VO_2^+}^s}{c_{VO_2^+}}\right]\left[\frac{c_{H^+}^s}{c_{H^+}}\right]^2 \exp\left[\frac{-\alpha F\eta_{ca}}{RT}\right] - \left[\frac{c_{VO^{2+}}^s}{c_{VO^{2+}}}\right]\exp\left[\frac{(1-\alpha)F\eta_{ca}}{RT}\right]\right) \qquad [46]$$

The applied current density can be obtained according to $j = S_{ca}V_{ca}j^{BV}/A_{ca}$, and the exchange current density was estimated by Equation 47. The dependency of the cathode rate constant with temperature can be expressed by an Arrhenius approach, Equation 48.

$$j_{0,ca}^{BV} = Fk_{ca}\left(c_{VO^{2+}}\right)^{\alpha}\left(c_{VO_2^+}c_{H^+}^2\right)^{(1-\alpha)} \qquad [47]$$

$$k_{ca} = k_{ca,ref}\exp\left(-\frac{FE_{ca,T_{ref}}^{\circ}}{R}\left[\frac{1}{T_{ref}} - \frac{1}{T}\right]\right) \qquad [48]$$

In the above equations, the term j^{BV} and $j_{0,ca}^{BV}$ are the current density and exchange current density (current per unit of surface area of pore walls), α is the transfer coefficient for the vanadium redox reaction (Equation 1), S_{ca} is the specific surface area of the cathode (surface area of pore walls per unit volume of total electrode) and c_i^s is the surface concentration of species i at the liquid–solid interface of the cathode. k_{ca} and $k_{ca,ref}$ are the rate constant and reference rate constant, T_{ref} is the reference temperature and $E_{ca,T_{ref}}^0$ is the standard potential at the reference temperature.

The Butler–Volmer equation presented in Equations 46 and 47 considers the mass transfer effects, which become more important at higher applied current densities or even for a small current density at high SOC conditions during charge–discharge operation. In order to evaluate the surface concentrations, the rate of electrode reaction (i.e., flux of species consumption/production according to Butler–Volmer equation) was matched to the rate at which electro-active species are brought to the surface by mass transfer,[76] Equations 49, 50 and 51. The rate of mass transfer was considered proportional to a linear concentration gradient at the surface of the electrode within a Nernst diffusion layer (δ_0).[30,41,45,76]

$$-\frac{D_{VO^{2+}}}{\delta_0}(c_{VO^{2+}} - c_{VO^{2+}}^s) = \frac{j^{BV}}{F} \qquad [49]$$

$$\frac{D_{VO_2^+}}{\delta_0}(c_{VO_2^+} - c^s_{VO_2^+}) = \frac{j^{BV}}{F} \quad [50]$$

$$\frac{D_{H^+}}{\delta_0}(c_{H^+} - c^s_{H^+}) = 2\left(\frac{j^{BV}}{F}\right) \quad [51]$$

The overpotential for the anode (η_{an}) was approximated by a Tafel-Volmer approach, which was utilized to describe the hydrogen oxidation/evolution reaction, since it has been reported that these reactions are not successfully represented by a Butler-Volmer relation.[35] Kinetic models considering two pathways with three elementary steps (i.e., Tafel, Heyrovsky and Volmer) are well established to develop the overall rate expression. Tafel-Volmer (TV) elementary steps include adsorption/desorption of reactant and product and the electron transfer reaction,[35] which are shown in Equations 52 and 53.

$$H_{2,surf} + 2S \underset{k_{des}}{\overset{k_{ad}}{\leftrightharpoons}} 2S - H_{ad} \quad [52]$$

$$S - H_{ad} \underset{k_{-V}}{\overset{k_V}{\leftrightharpoons}} S + H^+ - e^- \quad [53]$$

Where S is the surface adsorption site, $H_{2,surf}$ is the hydrogen molecule adjacent to the surface, k_{ad} and k_{des} are the adsorption and desorption rate constants of Tafel reaction, and k_V and k_{-V} are the forward and backward rate constants of the Volmer reaction.

A TV kinetic model that has been introduced by Kucernak et al.[35] was utilized in the proposed model, Equation 54. This equation describes the current density – overpotential relation as independent of the pH, and only dependent on the hydrogen partial pressure and kinetic rate constants under near mass-transport free conditions. The coverage of hydrogen on the electrode surface ($\theta^{TV}_{H_{ad}}$) is also a function of the hydrogen pressure and the overpotential (Equation 55). Crossover of vanadium species is expected to reduce the electro-active area in the anode by means of physisorption on the Pt catalyst competing with hydrogen adsorption, which will affect the current density of the cell. This loss in electro-active area must be included in the model by modifying the coverage of hydrogen on the electrode surface ($\theta^{TV}_{H_{ad}}$) and/or the roughness factor of the anode (R_{an}); however such an effect is not considered in the present model. The effect of temperature was considered in Equation 57, which assumes that the reaction is controlled by a single activation energy (E_a).[35] The parameters of the TV model reported at standard ambient temperature and pressure (SATP, $\oslash$) conditions, namely a temperature of 298.15 K and an absolute pressure of 1 bar, are given in Table III. The current density at standard conditions ($j^{TV,\oslash}$) is obtained using Equations 54 to 55 and the applied current density can be obtained according to $j = R_{an} j^{TV}$, where R_{an} is the roughness factor of the CL and j^{TV} is the current density at operating conditions (current per unit of electrochemically active area).

$$\frac{j^{TV}}{k_{des}} = FZ\left(\theta^{TV}_{H_{ad}} e^{\beta f \eta_{an}} - B\left(1 - \theta^{TV}_{H_{ad}}\right)e^{-(1-\beta) f \eta_{an}}\right) \quad [54]$$

$$\theta^{TV}_{H_{ad}} = \left[4B^2 + Z\left(e^{\beta f \eta_{an}} + Be^{-(1-\beta) f \eta_{an}}\right) - \left[16B^2 + \left(Z(e^{\beta f \eta_{an}} + Be^{-(1-\beta) f \eta_{an}})\right)^2 + 8BZ\left(Be^{\beta f \eta_{an}} + e^{-(1-\beta) f \eta_{an}}\right)\right]^{0.5}\right] / \left[4\left(B^2 - 1\right)\right] \quad [55]$$

where,

$$B = \left(\frac{a_{H_2} k_{ad}}{k_{des}}\right)^{0.5}, \quad Z = \frac{k^{eq}_V}{k_{des}}, \quad f = \frac{F}{RT} \quad [56]$$

$$j^{TV} = (1 - s_{CL}) j^{TV,\oslash} \exp\left(-\frac{E_{an}}{R}\left(\frac{1}{T} - \frac{1}{298.15}\right)\right) \quad [57]$$

In the above equations, β is the transfer coefficient of the hydrogen redox reaction (Equation 2) and a_{H_2} is the activity of dissolved hydrogen and equivalent to the change in partial pressure of hydrogen[35] according to $a_{H_2} = a^{\oslash}_{H_2}(p_{H_2}/p^{\oslash}_{H_2})$, where $a^{\oslash}_{H_2}$ and $p^{\oslash}_{H_2}$ are the standard state activity of hydrogen in solution and in the gas phase ($a^{\oslash}_{H_2} = 1$, $p^{\oslash}_{H_2} = 1$ bar).

Experimental

Experimental data was collected to validate the proposed model, galvanostatic tests were performed using an in-house manufactured RHVFC with a cross-sectional area of 25 cm^2. The cell consisted of polypropylene insulating layers, aluminum end plates, graphite flow channel plates and the MEA. The MEA contained a carbon electrode (SGL 10AA, 400 μm) and a platinised carbon paper electrode (Alfa Aesar Hydrogen Electrode, 200 μm, 0.5 mg cm^{-2} Pt loading), which were separated by a Nafion 117 membrane. Multi-channel serpentine flow channel plates (SGL, BMA5 graphite plates) were used as current collectors and to distribute the vanadium electrolyte as well as the hydrogen gas. To improve the current collection, copper current collectors were used between the polypropylene plates and flow channel plates in a previous set of experimental tests.[77] The catholyte solution was prepared by fully dissolving 14.1 g of vanadium sulfate hydrate (Sigma-Aldrich) in 60 mL of 5 M H_2SO_4 solution (Fluka Analytical). A peristaltic pump was used to circulate the vanadium catholyte between the cell and catholyte tank at a constant flow rate of 1.67×10^{-6} $m^3 s^{-1}$. Hydrogen was passed through the anode side at a constant flow rate of 1.67×10^{-6} $m^3 s^{-1}$. A collector reservoir was connected to the hydrogen outlet to collect any catholyte crossover.

The galvanostatic charge and discharge tests were performed using a Bio-Logic potentiostat (VSP-300) running EC-Lab software. Experiments were performed at constant current density in the range of 50—600 A m^{-2} and flow rate of catholyte and hydrogen in the range of 0.42—2.5 $\times 10^{-6}$ $m^3 s^{-1}$, allowing the cell to reach an upper cutoff potential of 1.3 V and a lower cutoff potential of 0.4 V. OCP measurements were performed after each galvanostatic charge-discharge step. Finally, the OCP behavior as a function of SOC was measured by charging or discharging on a series of steps at constant current density and measuring OCP after each step. The SOC of the cell was calculated by comparing the experimental capacity with the maximum theoretical capacity (100% SOC) and considering that fresh solution was used (0% SOC). A summary of the operating conditions used in the OCP test and the charge–discharge (ch-dch) tests used in this paper is presented in Table V.

Results and Discussion

The model equations described in Mathematical model section were developed and solved in MATLAB by means of an Ordinary Differential Equation (ODE) solver, with absolute and relative tolerance set at 1×10^{-6}. Additionally, the events option of the ODE solver was used to incorporate the restriction associated to Equation 28.[78] The simulation of a potential curve in Figure 5 took about 4 min on an Intel Xeon E5-1620v3, 64-bit workstation with 32 GB RAM. In the following subsections: Model validation - open circuit potential and Model validation - cell potential, the complete Nernst equation is fitted to experimental data of OCP, and the proposed model is validated against experimental data of cell potential during charge and discharge.

Model validation - open circuit potential.—The first step in the model validation is to fit the proposed complete Nernst equation, Equation 40, to the measured OCP. The initial species concentrations in the catholyte were calculated considering the vanadium sulfate hydrate, $VOSO_4 \cdot xH_2O$, contained 3.5 molecules of water.

During operation, the electron-transfer reaction and acid dissociation cause a change in the concentration of all species in the

Table V. Experimental data sets.

N°	test[a]	Current density $A\,m^{-2}$	Catholyte flow rate $10^{-6}\,m^3s^{-1}$	hydrogen flow rate $10^{-6}\,m^3s^{-1}$	Cu current collectors Yes or No
1	OCP	0	1.67	1.67	No
2	ch-dch	50	1.67	1.67	No
3	ch-dch	100	1.67	1.67	No
4	ch-dch	80	1.67	1.67	Yes
5	ch-dch	400	1.67	1.67	Yes
6	ch-dch	400	1.67	0.83	Yes
7	ch-dch	400	2.5	1.67	Yes
8	ch-dch	600	1.67	1.67	Yes

[a]Experimental test: OCP refers to open circuit potential test; and ch-dch refers to a test of a single charge-discharge cycle.

catholyte,[38] which were estimated as follows:

$$c_{VO^{2+}} = c_V \cdot (1 - SOC) \quad [58]$$

$$c_{VO_2^+} = c_V \cdot SOC \quad [59]$$

$$c_{H^+} = c^0_{H^+} + c_V \cdot SOC + S^{eq}_d \quad [60]$$

$$c_{HSO_4^-} = c^0_{HSO_4^-} - S^{eq}_d \quad [61]$$

$$c_{SO_4^{2-}} = c^0_{SO_4^{2-}} + S^{eq}_d \quad [62]$$

Where c_V is the total concentration of vanadium and c^0_i is the initial concentration of species i.

The proton, bisulphate and sulfate concentrations were assumed to follow a complete first step of dissociation of sulphuric acid (Equation 6), and a second step (Equation 7) according to a bi-sulfate dissociation constant (k_2) and an activity coefficient product (γ) as presented in Equation 8. For this purpose, the molar equilibrium dissociation quotient, $Q_M = k_2/\gamma$ presented in Figure 2 was used.

Figure 4a shows the E_{OCP} estimated by Equation 40 compared to one data set of experimental OCP. This Figure includes three different estimations: (1) a the Nernst Equation (NE), Equation 63, with unity activity coefficients, (2) a Complete Nernst Equation (CNE), Equation 40, with unity activity coefficients, and (3) a CNE considering non-ideal activity coefficients by means of a global activity coefficient (γ_{OCP}). The fitted values of γ_{OCP} against experimental data are shown is Figure 4b.

$$E^{NE}_{OCP} = E^{\circ}_{cell} + \frac{RT}{F}\ln\left(\frac{c^{ca}_{VO_2^+}(c^{ca}_{H^+})^2(p^{g}_{H_2})^{0.5}}{c^{ca}_{VO^{2+}}c^{an}_{H^+}}\right) \quad [63]$$

In the case of VRFBs, the Nernst equation with unity activity coefficients underestimates the OCP data and the Donnan potential across the membrane has been added in order to fit OCP data.[38] However, this potential difference should reduce the OCP when the catholyte concentration of protons is higher than the anolyte one, because a steady state condition must be maintained, i.e., no net flux of protons across the membrane.[42] This effect is contrary to the one presented by Knehr and Kumbur,[38] which increased the OCP in the case of all-vanadium cells because the equation considers the catholyte concentration of protons to the power of 3. On the other hand, Pavelka et al.[42] have presented a thermodynamic derivation of OCP for VRFBs that does not contain this cubic term, but instead the catholyte concentration of protons to the power of 1. They stated that for cation exchange membranes the non-ideal activity coefficients should be found or fitted against experimental data to improve the agreement.[42]

The OCP equation used in this work was derived as shown in Appendix A and is analogous to the derivation presented by Pavelka et al.[42] Similar effect to the described above is shown in Figure 4a, where the CNE with unity activity coefficients gives lower values of OCP in comparison to the NE curve. The fitted values of γ_{OCP} are shown in Figure 4b along with an empirical model of its dependency

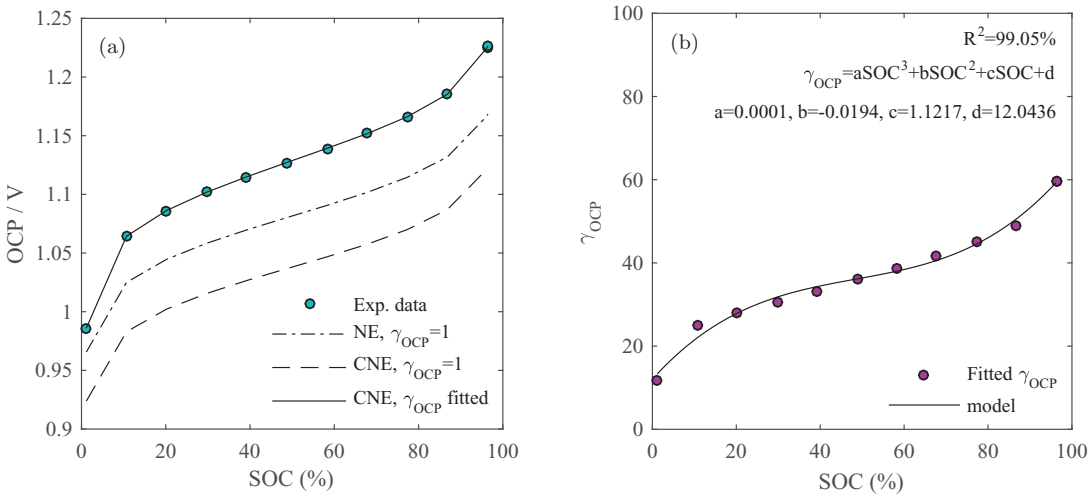

Figure 4. OCP at operating conditions presented in Table VI. (a) shows a comparison of Nernst equation (Equation 63) with unity activity coefficients, and a complete Nernst equation (Equation 40) with unity activity coefficients and fitted values of a global activity coefficient (γ_{OCP}), and (b) shows the fitted values of the global activity coefficient.

Table VI. Operating parameters and initial conditions.

Parameter	Symbol	Value	Unit	Source
Temperature	T	293	K	Measured
Current density	j	50—600	A m^{-2}	Measured
Flow rate of catholyte	Q_{ca-el}	1.67×10^{-6}	m^{3}s^{-1}	Measured
Inlet flow rate of hydrogen	$Q_{H_2,IN}$	1.67×10^{-6}	m^{3}s^{-1}	Measured
Total concentration of vanadium	c_V	1042	mol m^{-3}	Calculated
Initial SOC	SOC^0	0.1-5%	—	Estimated
Initial dissolved water concentration in CL	c^0_{dw}	9959	mol m^{-3}	Estimated (λ^{eq}_{CL} at $a_v = 1$)
Initial liquid saturation in CL	s^0_{CL}	0.1	—	Estimated
Initial liquid saturation in anode channel	c^0_{CH}	0	—	Estimated
Initial hydrogen concentration at anode side	$c^0_{H_2}$	41.4	mol m^{-3}	Calculated
Initial vapor concentration at anode side	c^0_v	0.99	mol m^{-3}	Estimated ($p_v = p^{sat}_v$)
Initial pressure in anode side	p^0_{an}	103351	Pa	Estimated

with SOC. The fitted values of the global activity coefficient vary between 10 to 60, which should be strongly related to the value of the activity coefficient of protons that have been reported to be of approximately 5 for a concentration of H_2SO_4 of 1 mol kg^{-1} and even higher for higher concentrations of H_2SO_4.[57] This analysis was repeated for each OCP experimental data set, which showed similar values for the fitted global activity coefficient. OCP experimental measurements were performed four times considering two different fresh solutions. A correct estimation of the OCP is key for the accuracy of model predictions and the estimation of overpotential contributions.

Model validation - cell potential.—The second step in the model validation is to compare the model prediction against the experimental potential data of charge and discharge. The fitting procedure was implemented in MATLAB using a non-linear least-squares solver (lsqcurvefit function), which allowed upper and lower boundaries for the fitting parameters to be set. In principle any model parameter could be taken as a free fitting parameter, but its value should be maintained within the physically meaningful limits.[79] Common fitting parameters used in VRFB models are reaction rate constants, ionic or electronic conductivities, electrode specific surface areas, charge transfer coefficients, diffusion coefficients and permeabilities.[10,30,39,45,46] It is important to select realistic initial values of the fitting parameters to decrease the solution uncertainty since the solver algorithm does not necessarily find a global optimum or unique solution.[79] To this end, the fitting parameters were chosen to be the standard reaction rate constant for the cathode ($k_{ca,ref}$), the Nernst diffusion layer (δ_0) and an extra ohmic resistance (R_C). Their initial values were selected as $k_{ca,ref}$=8.1 × 10^{-7} ms^{-1},[80] δ_0=50.3 × 10^{-6} m which is the mean pore radius (r_p),[30] and R_C=5 Ω cm^2[27] for the cell without Cu current collectors and R_C=0.5 Ω cm^2 for the cell with Cu current collectors. Their lower and upper boundaries were selected as 10^{-10} and 10^{-6} m s^{-1} for $k_{ca,ref}$, $r_p/10$ and $2r_p$ for δ_0 and, 3 and 6 Ω cm^2 for R_C for the cell without Cu current collectors, while 0.01 and 1 Ω cm^2 for R_C for the cell with Cu current collectors. The decision of including an additional resistance was based in previous measurements[7] which showed a series resistance (R_S) of around 5 Ω cm^2 at a catholyte flow rate of 1.67×10^{-6} m^{3}s^{-1} using the same experimental set-up (cell, assembly, supplies, etc.) that the one used in this work without Cu current collectors, while a series resistance of around 0.8 Ω cm^2 with Cu current collectors.

The fitting of the model was carried out against one single cycle experimental data at a current density of 400 A m^{-2} and then simulations were carried out using the obtained fitting parameters to validate the model under different current densities, as reported in Figures 5 to 7. The only parameter refitted was R_C, depending if the tests were done with or without Cu current collectors. The simulations were performed following the actual operation of the cell, setting the initial SOC at a very small value (0.1%) in the cases where fresh catholyte solution was used or to an estimate value of initial SOC usually between 0 and 5%, calculated based on the experimental data. The initial concentration of species and the operating parameters that were considered in the simulation are given in Table VI.

Figure 5 presents the model calibration against experimental charge and discharge potential curves at a current density of 400 A m^{-2}, Table V data set N°5, for the cell with Cu current collectors. During the model fitting, it was noticed that the fitting error was mainly due to the differences at the final part of the discharge curve (SOC<20%), and therefore, larger weighting factors were attributed to the charge curve and the beginning of the discharge curve during the model fitting process to allow for a more sensible identification of fitting parameters. The fitted parameters obtained were $k_{ca,ref}$=1.2 × 10^{-7} ms^{-1}, δ_0=84.8 × 10^{-6} m and R_C=0.3 Ω cm^2. Although, the best fit could not remove all the discrepancies between the experimental data and the model simulation, a reasonably good agreement was observed with a total RMSE of 3.6% and 5.4% during charge and discharge, respectively. It can be seen that the error for the charge simulation is mainly produced by differences at extreme conditions and the high error for the discharge simulation is mainly due to the differences at low SOC, which are less critical for practical applications. It is worth noting that the rate of depletion of active species in the cathode is sensitive to the flow rate penetration into the cathode, which was calculated by a simplified model (Mathematical model section) along with the assumption that only the fraction of catholyte flow rate through the cathode participate in the reaction. This may well be responsible for most of the differences during discharge.

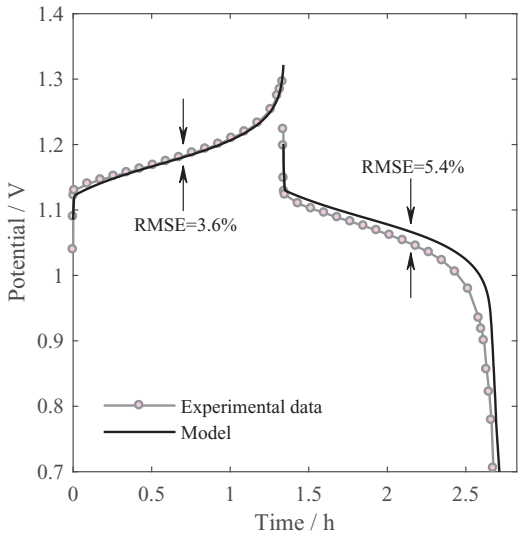

Figure 5. Model calibration against experimental data at a current density of 400 A m^{-2} and flow rate of catholyte and hydrogen of 1.67 × 10^{-6} m^{3}s^{-1}, data set N°5.

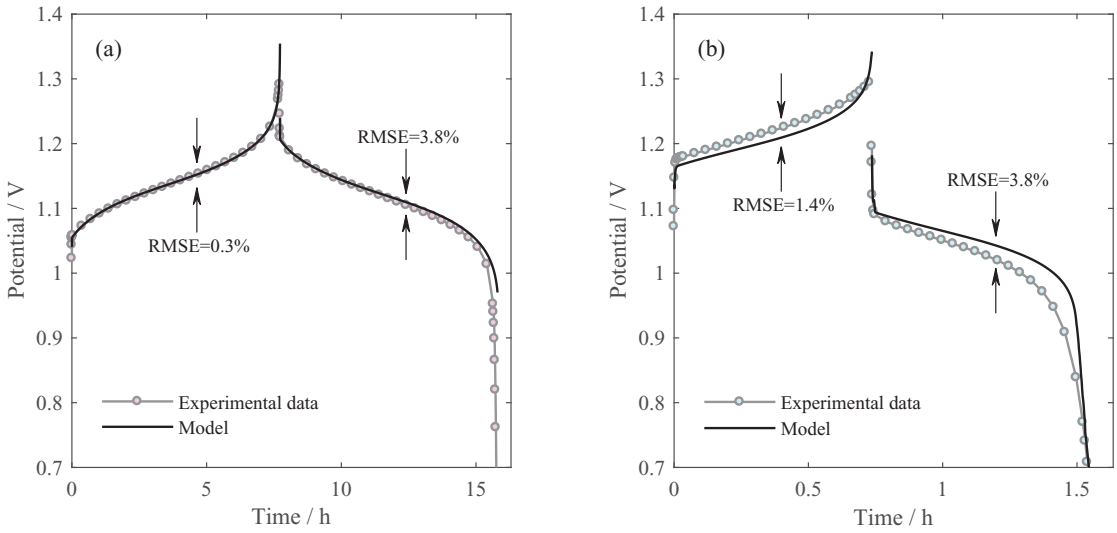

Figure 6. Model validation by using the same fitted parameters against experimental data at a flow rate of catholyte and hydrogen of 1.67×10^{-6} $m^3 s^{-1}$ and a current density of (a) 80 A m^{-2} data set N°4, and (b) 600 A m^{-2} data set N°8.

Additionally, the assumption of unity activity coefficients (Assumption 5) and neglected effects such as the transport of vanadium and H_2SO_4 species through the membrane into the CL and changes of water content in the catholyte could explain to some degree the difference between the model and experimental data. Self discharge and gas evolving reactions are not considered in the model, which are expected to decrease the coulombic efficiency in the experimental case.

After the model calibration, the parameters $k_{ca,ref}$, δ_0 and R_C were used to simulate the cell performance at 80 and 600 A m^{-2}, Table V data set N°4 and N°8, respectively. The model demonstrated good accuracy in representing the performance of the cell at both current densities. Figure 6 shows the validation of the model by comparing the simulated cell performance and the experimental data at 8 and 600 A m^{-2}, which produced a RMSE of 0.3% and 3.8% during charge and discharge at 8 A m^{-2} and a RMSE of 1.4% and 3.8% during charge and discharge at 600 A m^{-2}. An increase in the discrepancy between the model and the experimental data occurs at the beginning of discharge when a higher current density was used, which may respond to an overestimation of the average concentration of species in the cathode. The parameter R_C was refitted to be able to simulate the experimental data at 50 and 100 A m^{-2} of the cell without Cu current collector, Table VI data sets N°2 and N°3. The refitted R_C took the value R_C=3.6 Ω cm^2. The model demonstrated good agreement with the experimental data at both current densities. Figure 7 shows the validation of the model by comparing the simulated cell performance and the experimental data at 50 and 100 A m^{-2}, which produced a RMSE of 1.6% and 2.0% during charge and discharge at 50 A m^{-2} and a RMSE of 0.7% and 1.8% during charge and discharge at 100 A m^{-2}. It can be noticed the effect of the extra ohmic resistance, which produce an increase of approximately 60 mV of the potential curve at 100 A m^{-2} compared with the curve at 80 A m^{-2} over the linear range of performance. On the other hand, validation of the model at different flow rates of catholyte and hydrogen (data sets N°6 and N°7) can be seen in Figure 8. The model was able to simulate the performance of the cell when different flow rates were used.

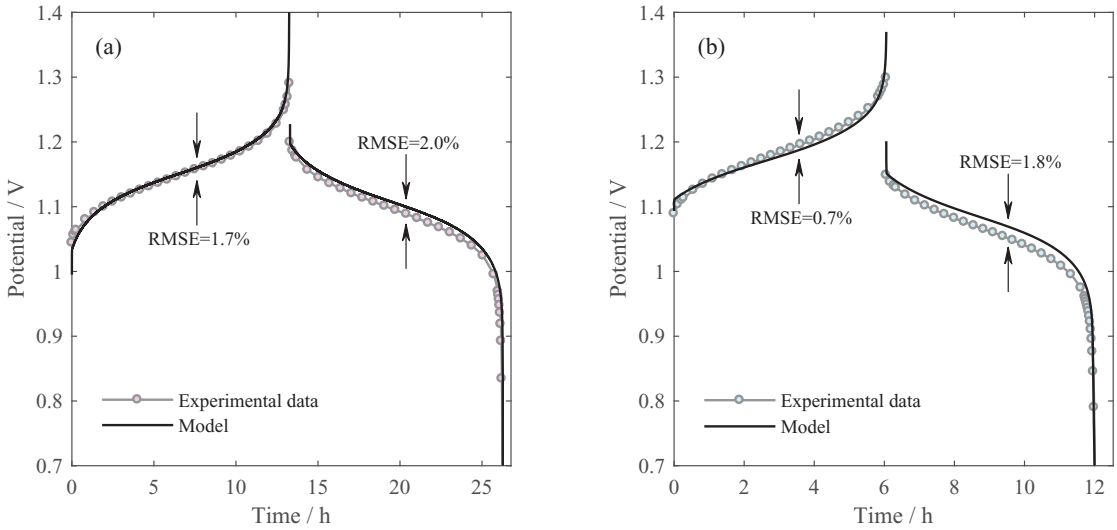

Figure 7. Model validation, using refitted R_C, against experimental data at a flow rate of catholyte and hydrogen of 1.67×10^{-6} $m^3 s^{-1}$ and a current density of (a) 50 A m^{-2} data set N°2, and (b) 100 A m^{-2} data set N°3.

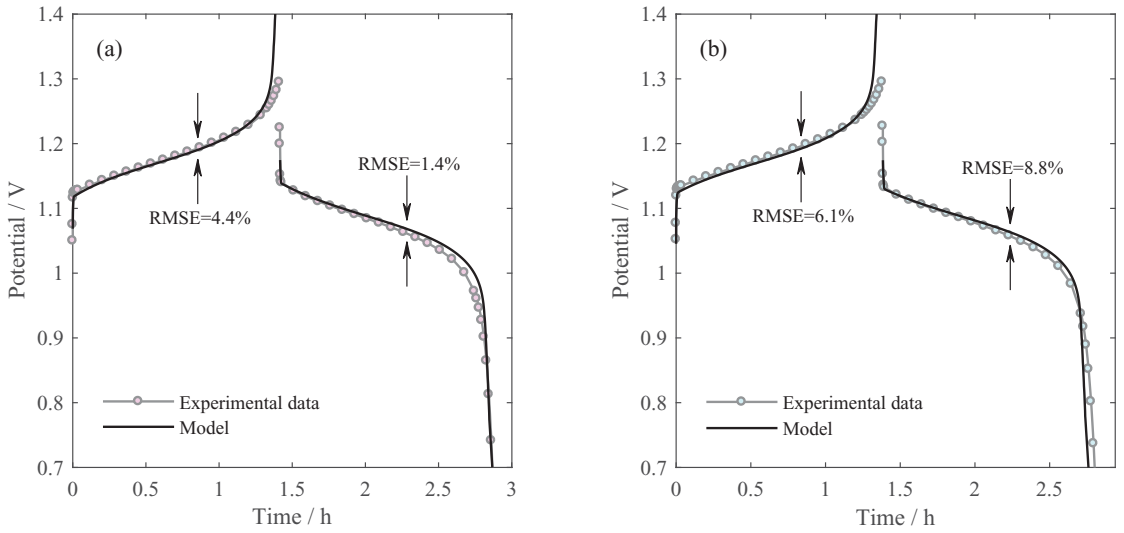

Figure 8. Model validation by using the same fitted parameters against experimental data at a current density of 400 A m^{-2} and flow rates of: (a) 2.5×10^{-6} $m^3 s^{-1}$ of catholyte and 1.67×10^{-6} $m^3 s^{-1}$ of hydrogen, data set N°7; and (b) 1.67×10^{-6} $m^3 s^{-1}$ of catholyte and 0.83×10^{-6} $m^3 s^{-1}$ of hydrogen, data set N°6.

Evolution of species in electrodes.—The results of the evolution of species in the cathode and anode for the experimental data at a current density of 50 A m^{-2} (data set N°2) is presented in Figures 9 and 10. The evolution of the species concentration in the cathode during charge and discharge mode is presented in Figure 9. The concentration of vanadium species VO^{2+} and VO_2^+ based on Equations 9 and 10 and the concentration of sulphuric species based on Equations 11, 12 and 13 are presented in Figures 9a and 9b, respectively. The species concentrations presented a linear rate of change, which is reached at around 70 s for the operating conditions. The rate of change of the species concentrations depends on the stoichiometric coefficients and number of electrons consider in the redox reactions, along with the flow rate penetration to the domain as it can be noticed in Equation 9 to 13. In the particular case of protons, 2 moles of H^+ are generated in the catholyte with respect to 1 mole of VO_2^+ during charge, and it would be expected that its concentration increases with this same proportion. However, the concentration of protons in the catholyte is affected because 1 mole of protons must be transported across the membrane to participate in the anode reaction and the chemical dissociation of HSO_4^- also takes place in the electrolyte. It can be seen in Figure 9b that the concentration of SO_4^{2-} and HSO_4^- change during charge and discharge operation, which is explained by the condition of equilibrium of the reaction of HSO_4^- dissociation, Equation 7. On the other hand, the effect of the flow rate penetration can be illustrated if a lower flow rate penetration is allowed, a faster rate of change of ionic concentrations would be expected. The error produced by the simplified model used to obtain the flow rate penetration into the cathode is acceptable for the discrepancies observed between experimental data sets and the simulations (Figures 5 to 8). The error is expected to increase if higher current densities are used, in which case the model should be extended to include spatial distribution effects, i.e., One or Two Dimensional (1D or 2D) model, allowing the actual species flux into the cathode and across the membrane to be calculated.

The evolution of the species concentration in the anode CL during charge and discharge mode at a current density of 50 A m^{-2} is presented in Figure 10. The concentration of vapor and hydrogen based on Equations 20 and 23 and the liquid water saturation and water content based on Equations 21 and 22 are presented in Figures 10a

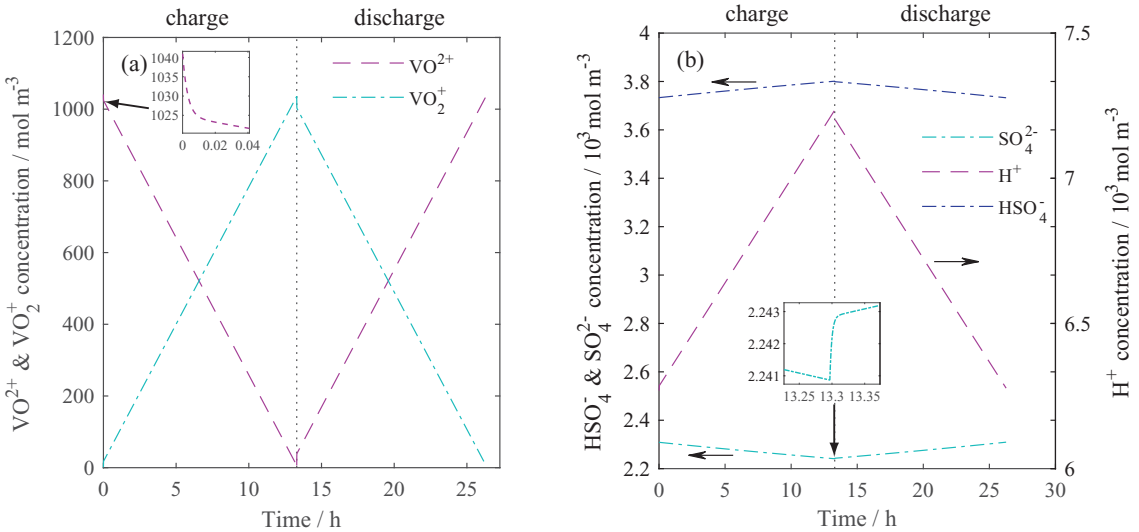

Figure 9. Evolution of species concentration against time in the cathode during charge and discharge at a current density of 50 A m^{-2} and a flow rate of catholyte and hydrogen of 1.67×10^{-6} $m^3 s^{-1}$, data set N°2: (a) shows the vanadium species VO^{2+} and VO_2^+ and (b) shows the sulphuric acid species H^+, SO_4^{2-} and HSO_4^-.

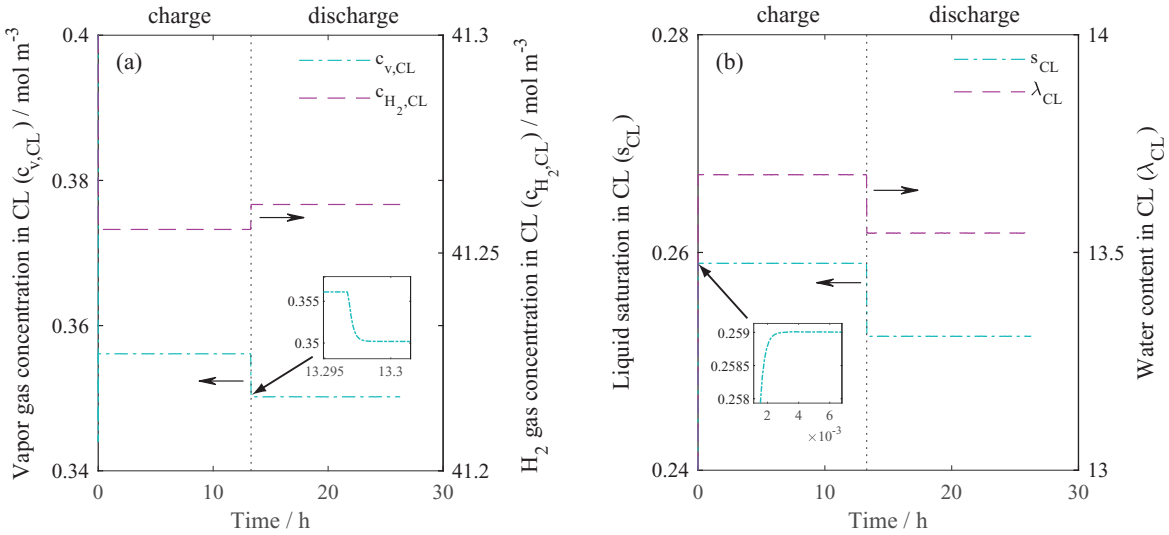

Figure 10. Evolution of species concentration against time in the CL during charge and discharge at a current density of 50 A m^{-2} and a flow rate of catholyte and hydrogen of 1.67×10^{-6} m^{3}s^{-1}, data set N°2: (a) shows vapor and hydrogen concentrations and (b) shows the liquid water saturation (s_{CL}) and water content in the polymer electrolyte (λ_{CL}).

and 10b, respectively. All species concentrations in the anode CL presented a steady-state behavior, which is reached in around 10 s for the operating conditions. This initial transient behavior is in response to the water transport through the membrane and the phase change processes of liquid water desorption and evaporation/condensation. It was observed that during discharge the liquid saturation slightly decreased with respect to its value during charge, possibly due to the change of direction of the electro-osmotic drag flux toward the cathode while the diffusion flux maintained its direction toward the anode. It is worth noting that the simulation results somewhat overestimated the amount of water lost from the catholyte tank with respect to the experimental observations. During the experimental operation of a single cycle of charge and discharge at a low current density, the total crossover solution collected from the outlet of the anode channel was marginal compared with the catholyte volume. The dark blue color of this crossover solution suggested that vanadium species were also transported across the anode side and left the system. Tang et al.[74] have observed sulphuric acid and vanadium uptake in membranes after equilibration with solutions of sulphuric acid and vanadyl sulfate. They reported a reduction to some extend of the membrane conductivity, proton mobility and water content in electrolytes with a typical composition of VRFB feed, suggesting a complicated equilibrium and partitioning competition between protons and vanadyl.[74] A detailed model of the simultaneous transport of species across the membrane was not explored in this study. Moreover, it is important to note that if different operating conditions were used as higher current densities, it is possible to produce flooding of the anode side. Further study is currently ongoing to describe the water and ionic species transport across the membrane and to estimate their effect on the anode performance.

Conclusions

This study introduced a time-dependent model for a RHVFC considering mass conservation and electrochemical processes. A well-established modeling approach has been used to describe a RHVFC by means of coupling physicochemical phenomena used to simulate the performance of different systems, such as VRFBs and PEMFCs. The model was validated considering experimental data of OCP and cell potential. The OCP data was fitted with a complete Nernst equation that was derived from thermodynamics, considering a global activity coefficient. The simulated cell potential, considering the overpotential of cathode and anode and the ohmic losses, was compared to charge–discharge cycle data sets showing a good degree of accuracy in predicting the cell performance. The discrepancy between experimental data and the model simulations at the end of charge and discharge is most likely explained by the the use of a simplified model to estimate the catholyte flow rate penetration into the cathode domain, which may predict a slower rate of change of active species concentration. The discrepancies at extreme conditions (10%>SOC or SOC>90%) could be explained by the use of unity activity coefficients in the kinetic relations, i.e., Butler-Volmer relation for the positive side and Tafel-Volmer relation for the negative side. Moreover, self discharge, gas evolving reactions and crossover of ionic species through the membrane have been neglected in the proposed model, which may well affect the performance of the cell. The model is capable of representing the voltage dynamics observed in a RHVFC at moderate current densities, considering the range of operating conditions used to validate it. However, the use of the model to predict performance at conditions beyond the validation range implemented in this paper might not produce meaningful results and significant further experimental data would be required.

The model presented in this study can be used as a first approximation, allowing simulation of the system and providing a foundation for further development of physical-based models for regenerative fuel cells. In addition, the electrochemical approaches used in the model may serve as reference for studying similar systems, such as all-vanadium and H_2/Br_2, which may benefit from the complete Butler-Volmer equation for the cathode considering VO^{2+}, VO_2^+ and H^+, the complete Nernst equation and the kinetic approach for the hydrogen oxidation/evolution reaction used in this study. Further research will include RHVFC testing under a wider range of operating conditions and the corresponding model validation. The contribution of effects such as spatial distribution in the electrodes, ionic species crossover, and water transport through the anode, will be significant under high current density operation. Modifications to the proposed model by incorporating a more detailed water management model, transport of cathode ionic species through the membrane and their interaction with the CL as well as study on species spatial distribution (1D to 2D approaches) need to be further investigated. The low-complexity modeling approach used in this paper has enhanced the understanding of the system performance by coupling physical and electrochemical processes occurring in the RHVFC, enabling identification of the key phenomena and highlighting areas requiring future in-depth study.

Acknowledgments

The authors acknowledge BECAS CHILE–CONICYT, Ministry of Education Chile Scholarship and EPSRC UK grants EP/L019469/1 and EP/K002252/1 for funding this work. We would like to express our appreciation to Dr. Antonio Bertei for all the useful discussions and constant support during the course of this research, more specifically his guidance in the derivation of the electrochemical relations and his comments that helped to improve the manuscript significantly. We are also immensely grateful to Dr. Samuel Cooper for his comments on an early version of the manuscript.

List of Symbols

a_i	activity of species i
A	cross-sectional area, m^2
c_i	concentration of species i, mol m^{-3}
c_V	total concentration of vanadium, mol m^{-3}
c°	standard molarity, mol L^{-1}
$D_{Kn,i}$	Knudsen diffusion coefficient of species i, m^2 s^{-1}
$D_{i,j}$	binary diffusion coefficient of species i and j, m^2 s^{-1}
d_p	mean pore size, m
d_f	mean fiber diameter, m
d	pipe diameter, m
$D_{i,k}$	diffusion coefficient of species i in domain k, m^2 s^{-1}
D_h	hydraulic diameter, m
E°	standard potential, V
EW	equivalent molecular weight of polymer electrolyte membrane, kg $mol^{-1}{}_{SO3H}$
E_a	activation energy, kJ mol^{-1}
E	potential, V
f_V	volume fraction of water in the membrane
f_F	Fanning friction factor
f_{CH}	friction resistance coefficient of the channel
F	Faraday's constant, 96 485 C
G	mass flux, kg m^{-2} s^{-1}
h	height, m
j_0	exchange current density, A m^{-2}
j	current density, A m^{-2}
k_c	condensation rate constant, s^{-1}
k_e	evaporation rate constant, atm^{-1} s^{-1}
k_B	Boltzmann constant, m^2kg s^{-2} K^{-1}
k_{ca}	cathode rate constant, m s^{-1}
k_1	Sulfuric acid dissociation coefficient
k_2	Bi-sulfate dissociation coefficient
k_{ad}	adsorption rate constant, mol cm^{-2} s^{-1}
k_{des}	desorption rate constant, mol cm^{-2} s^{-1}
k_V	forward rate constant of Volmer reaction, mol cm^{-2} s^{-1}
k_{-V}	backward rate constant of Volmer reaction, mol cm^{-2} s^{-1}
K	permeability, m^2
K_f	minor resistance coefficient
K_{KC}	Kozeny-Carman constant
l_k	thickness of domain k, m
L_{CH}	channel length, m
L_{ca}	cathode flow length, m
L	pipe length, m
M	gas molecular weight, kg mol^{-1}
M_i	molecular weight of species i, kg mol^{-1}
$\dot{n}_i$	molar flow rate of species i, mol s^{-1}
N_i	molar flux of species i, mol m^{-2} s^{-1}
p	pressure, Pa
p_i	partial pressure of species i, Pa
Q	flow rate, m^3 s^{-1}
Q_M	molar equilibrium dissociation quotient
r_p	mean pore radius, m
R_C	extra ohmic resistance, Ω cm^2
R_w	phase change rate, mol s^{-1}
R_s	series resistance, Ω cm^2
R	universal gas constant, 8.314 J mol^{-1} K^{-1}
R_{an}	roughness factor of CL, m^2 m^{-2}
Re	Reynolds number
s	liquid saturation
S_d	dissociation reaction term, mol s^{-1}
S_{ca}	specific area of reaction in cathode, m^2 m^{-3}
t	time, s
T	temperature, K
v_m	mean velocity of the fluid, m s^{-1}
V	volume, m^3
V_m	molar volume of dry membrane, m^3 mol^{-1}
V_w	molar volume of water, m^3 mol^{-1}
w	width, m
y_i	molar fraction of species i
z_i	charge number of species i

Greek

α	transfer coefficient of cathode reaction
β	transfer coefficient of anode reaction
γ_{des}	electrolytic desorption rate coefficient in CL, s^{-1}
γ_i	activity coefficient of species i
γ_{OCP}	global activity coefficient term for OCP
γ	activity coefficient product
Δ	difference, drop
δ_0	Nernst diffusion layer, m
ε	porosity or volume fraction
$\epsilon_{i,j}$	characteristic binary Lennard-Jones energy, m^2kg s^{-2}
ϵ_i	characteristic Lennard-Jones energy of species i, m^2kg s^{-2}
η	overpotential, V
θ	hydrogen coverage
κ	effective permeability of the cathode
λ	content of water, mol of water per mol of sulphonic acid sites
μ	dynamic viscosity, kg m^{-1} s^{-1}
μ_i°	standard chemical potential if species i
μ_i	chemical potential if species i
$\tilde{\mu}_i$	electrochemical potential of species i
ξ_{drag}	electro-osmotic drag coefficient
ρ	density, kg m^{-3}
σ_i	molecular radii of species i, Å
σ_k	conductivity of domain k, S m^{-1}
$\sigma_{i,j}$	characteristic binary Lennard-Jones length, Å
τ	tortuosity
ϕ^k	potential of phase k, V
Ω_D	diffusion collision integral

Subscripts and Superscripts

0	initial value of variable ($t = 0$)
1	initial position in a pipe
2	final position in a pipe
an-el	anolyte
an	anode
BV	Butler-Volmer
CH	anode channel
ca-el	catholyte
c-m	cathode-membrane interface
ca	cathode
CL	catalyst layer
CL-m	polymer electrolyte in the membrane
cc	current collector
des	desorption
dm	dry membrane
diff	diffusion
dw	dissolved water

Don	Donnan potential
eq	equilibrium property
eff	Effective property
EO	electro-osmotic drag
f	fixed charge
GDL	gas diffusion layer
H_{ad}	adsorbed hydrogen
IN	inlet
k	domain k
m	membrane
M, M'	metal phase
NE	Nernst equation
OUT	outlet
Ohm	Ohmic loss
OCP	open circuit potential
react	electron-transfer reaction
ref	reference
s, surf	surface
sat	saturation
SATP	standard ambient temperature and pressure condition
T_{ref}	reference temperature, K
T	tank
TV	Tafel-Volmer
v	water vapor
V	Volmer reaction
wv	evaporation/condensation
w	liquid water

Appendix A: OCP Derivation

The measured OCP is the difference in electrochemical potential of electrons in the two terminals of a battery.[42,81] The electrochemical potential of a species i ($\tilde{\mu}_i$) is given by Equation A1, which considers the chemical potential of species i (μ_i) and the effect of potential (ϕ) on a charged species.

$$\tilde{\mu}_i = \mu_i + z_i F\phi \quad [A1]$$

Where the chemical potential of species i can be expressed in terms of the standard chemical potential (μ_i°) and activity of species i as,

$$\mu_i = \mu_i^\circ + RT\ln(a_i) \quad [A2]$$

$$a_i = \gamma_i c_i \quad [A3]$$

At equilibrium, each half-cell reaction presented in Equations 1 and 2 can be written in terms of electrochemical potentials as follows:

$$2\tilde{\mu}^{ca}_{VO_2^+} + 4\tilde{\mu}^{ca}_{H^+} + 2\tilde{\mu}^{CP}_{e^-} = 2\tilde{\mu}^{ca}_{VO^{2+}} + 2\tilde{\mu}^{ca}_{H_2O} \quad [A4]$$

$$\tilde{\mu}^{an}_{H_2} = 2\tilde{\mu}^{an}_{H^+} + 2\tilde{\mu}^{Pt}_{e^-} \quad [A5]$$

Considering, the equilibrium condition between the phases in contact and using Equation A1 to express the electrochemical potentials in the above equations.

$$F(\phi^M - \phi^{ca}) = \mu^{ca}_{VO_2^+} + 2\mu^{ca}_{H^+} + \mu^{M}_{e^-} - \mu^{ca}_{VO^{2+}} - \mu^{ca}_{H_2O} \quad [A6]$$

$$F(\phi^{M'} - \phi^{an}) = \mu^{an}_{H^+} + \mu^{M'}_{e^-} - \frac{1}{2}\mu^{an}_{H_2} \quad [A7]$$

Where M and M' represent the phase of the wires used to connect the voltmeter to the terminals of the battery. Subtracting Equation A7 to Equation A6.

$$F(\phi^M - \phi^{M'}) = \mu^{ca}_{VO_2^+} + 2\mu^{ca}_{H^+} - \mu^{ca}_{VO^{2+}} - \mu^{ca}_{H_2O} - \mu^{an}_{H^+} + \frac{1}{2}\mu^{an}_{H_2} + F(\phi^{ca} - \phi^{an}) \quad [A8]$$

The difference of potential of the electrolytes (Equation A9) can be obtained recognizing the steady state condition,[42] which leads to the equality of electrochemical potential of protons between both electrolytes.

$$F(\phi^{ca} - \phi^{an}) = \mu^{an}_{H^+} - \mu^{ca}_{H^+} \quad [A9]$$

This same relation can be obtained by considering the Donnan potential in the two electrolyte – membrane interfaces.[43,44] At equilibrium, the electrochemical potential of protons in the electrolyte and membrane must be the same. This was expressed for each interface as,

$$-F(\phi^m - \phi^{ca}) = \mu^m_{H^+} - \mu^{ca}_{H^+}$$
$$-F(\phi^m - \phi^{an}) = \mu^m_{H^+} - \mu^{an}_{H^+} \quad [A10]$$

then, the potential across the entire membrane, namely the dialysis potential (E^m_{Don}), was constructed.

$$FE^m_{Don} = F(\phi^{ca} - \phi^{an}) = \mu^{an}_{H^+} - \mu^{ca}_{H^+} \quad [A11]$$

To write the cell OCP, Equation A9 was substituted in Equation A8, and the chemical potentials were expressed with respect to Equation A2.

$$E_{OCP} = E^\circ_{cell} + \frac{RT}{F}\ln\left(\frac{a^{ca}_{VO_2^+}a^{ca}_{H^+}(a^{an}_{H_2})^{0.5}}{a^{ca}_{VO^{2+}}a^{ca}_{H_2O}}\right) \quad [A12]$$

where the standard cell potential was defined as,[42]

$$E^\circ_{cell} = \frac{1}{F}\left(\mu^{\circ,ca}_{VO_2^+} - \mu^{\circ,ca}_{VO^{2+}} - \mu^{\circ,ca}_{H_2O}\right) = 0.99V \quad [A13]$$

ORCID

H. Hewa Dewage https://orcid.org/0000-0002-0089-103X

References

1. M. Skyllas-Kazacos, M. H. Chakrabarti, S. A. Hajimolana, F. S. Mjalli, and M. Saleem, *Journal of The Electrochemical Society*, **158**(8), R55 (2011).
2. Z. Yang, J. Zhang, M. C. W. Kintner-Meyer, X. Lu, D. Choi, J. P. Lemmon, and J. Liu, *Chemical Reviews*, **111**(5), 3577 (2011).
3. P. Alotto, M. Guarnieri, and F. Moro, *Renewable and Sustainable Energy Reviews*, **29**, 325 (2014).
4. H. Chen, T. N. Cong, W. Yang, Ch. Tan, Y. Li, and Y. Ding, *Progress in Natural Science*, **19**(3), 291 (2009).
5. V. Yufit, B. Hale, M. Matian, P. Mazur, and N. P. Brandon, *Journal of The Electrochemical Society*, **160**(6), A856 (2013). Y. V. Tolmachev and M. A. Vorotyntsev, Russian Journal of Electrochemistry, 50(5), 403 (2014)
6. Y. V. Tolmachev and M. A. Vorotyntsev, *Russian Journal of Electrochemistry*, **50**(5), 403 (2014).
7. H. Hewa Dewage, V. Yufit, and N. P. Brandon, *Journal of The Electrochemical Society*, **163**(1), A5236 (2016).
8. Ch. L. Chen, University of Malaya, 2015.
9. Ch. L. Chen, H. K. Yeoh, and M. H. Chakrabarti, *Electrochimica Acta*, **120**, 167 (2014).
10. D. You, H. Zhang, and J. Chen, *Electrochimica Acta*, **54**(27), 6827 (2009).
11. D. M. Bernardi and M. W. Verbrugge, *AIChE Journal*, **37**(8), 1151 (1991).
12. D. M. Bernardi and M. W. Verbrugge, *Journal of The Electrochemical Society*, **139**(9), 2477 (1992).
13. X. You, Q. Ye, T. Van Nguyen, and P. Cheng, *Journal of The Electrochemical Society*, **163**(3), A447 (2016).
14. A. Z. Weber and J. Newman, *Chemical Reviews*, **104**(10), 4679 (2004).
15. C. Siegel, *Energy*, **33**(9), 1331 (2008).
16. A. A. Shah, K. H. Luo, T. R. Ralph, and F. C. Walsh, *Electrochimica Acta*, **56**(11), 3731 (2011).
17. A. Z. Weber, M. M. Mench, J. P. Meyers, P. N. Ross, J. T. Gostick, and Q. Liu, *Journal of Applied Electrochemistry*, **41**(10), 1137 (2011).
18. Q. Zheng, X. Li, Y. Cheng, G. Ning, F. Xing, and H. Zhang, *Applied Energy*, **132**, 254 (2014).
19. K. Jiao and X. Li, *Progress in Energy and Combustion Science*, **37**(3), 221 (2011).
20. T. E. Springer, T. A. Zawodzinski, and S. Gottesfeld, *Journal of the Electrochemical Society*, **138**(8), 2334 (1991).
21. S. Ge, X. Li, B. Yi, and I. Hsing, *Journal of The Electrochemical Society*, **152**(6), A1149 (2005).
22. Q. Ye and T. V. Nguyen, *Journal of The Electrochemical Society*, **154**(12), B1242 (2007).
23. A. A. Shah, G. S. Kim, P. C. Sui, and D. Harvey, *Journal of Power Sources*, **163**(2), 793 (2007).
24. H. Wu, P. Berg, and X. Li, *Journal of The Electrochemical Society*, **157**(1), B1 (2010).
25. W. He, J. S. Yi, and T. V. Nguyen, *AIChE Journal*, **46**(10), 2053 (2000).
26. D. Natarajan and T. V. Nguyen, *Journal of The Electrochemical Society*, **148**(12), A1324 (2001).
27. H. Wu, X. Li, and P. Berg, *Electrochimica Acta*, **54**(27), 6913 (2009).
28. C. Sun, J. Chen, H. Zhang, X. Han, and Q. Luo, *Journal of Power Sources*, **195**(3), 890 (2010).
29. A. Tang, J. Bao, and M. Skyllas-Kazacos, *Journal of Power Sources*, **196**(24), 10737 (2011).
30. K. W. Knehr, E. Agar, C. R. Dennison, A. R. Kalidindi, and E. C. Kumbur, *Journal of the Electrochemical Society*, **159**(9), A1446 (2012).
31. K. W. Knehr and E. C. Kumbur, *Electrochemistry Communications*, **23**, 76 (2012).
32. S. Won, K. Oh, and H. Ju, *Electrochimica Acta*, **177**, 310 (2015).

33. R. M. Darling, A. Z. Weber, M. C. Tucker, and M. L. Perry, *Journal of The Electrochemical Society*, **163**(1), A5014 (2016).
34. M. C. Tucker, K. T. Cho, F. B. Spingler, A. Z. Weber, and G. Lin, *Journal of Power Sources*, **284**, 212 (2015).
35. A. R. J. Kucernak and C. M. Zalitis, *The Journal of Physical Chemistry C*, **120**(20), 10721 (2016).
36. S. Chen and A. Kucernak, *The Journal of Physical Chemistry B*, **108**(10), 3262 (2004).
37. J. X. Wang, T. E. Springer, and R. R. Adzic, *Journal of The Electrochemical Society*, **153**(9), A1732 (2006).
38. K. W. Knehr and E. C. Kumbur, *Electrochemistry Communications*, **13**(4), 342 (2011).
39. E. Agar, K. W. Knehr, D. Chen, M. A. Hickner, and E. C. Kumbur, *Electrochimica Acta*, **98**, 66 (2013).
40. W. W. Yang, Y. L. He, and Y. S. Li, *Electrochimica Acta*, **155**, 279 (2015).
41. Y. A. Gandomi, D. S. Aaron, T. A. Zawodzinski, and M. M. Mench, *Journal of The Electrochemical Society*, **163**(1), A5188 (2016).
42. M. Pavelka, F. Wandschneider, and P. Mazur, *Journal of Power Sources*, **293**, 400 (2015).
43. K. Kontturi, L. Murtomaki, and J. A. Manzanares, *Ionic Transport Processes: In Electrochemistry and Membrane Science*, Oxford University Press Inc., New York (2008).
44. C. H. Hamann, A. Hamnett, and W. Vielstich, *Electrochemistry*, WILEY-VCH Verlag GmbH & Co. KGaA, Weinheim (2007).
45. A. A. Shah, M. J. Watt-Smith, and F. C. Walsh, *Electrochimica Acta*, **53**(27), 8087 (2008).
46. A. A. Shah, R. Tangirala, R. Singh, R. G. A. Wills, and F. C. Walsh, *Journal of The Electrochemical Society*, **158**(6), A671 (2011).
47. A. Tang, S. Ting, J. Bao, and M. Skyllas-Kazacos, *Journal of Power Sources*, **203**, 165 (2012).
48. A. Tang, J. Bao, and M. Skyllas-Kazacos, *Journal of Power Sources*, **216**, 489 (2012).
49. D. You, H. Zhang, C. Sun, and X. Ma, *Journal of Power Sources*, **196**(3), 1578 (2011).
50. M. Skyllas-Kazacos and L. Goh, *Journal of Membrane Science*, **399–400**, 43 (2012).
51. B. Xiong, J. Zhao, K. J. Tseng, M. SkyllasKazacos, T. M. Lim, and Y. Zhang, *Journal of Power Sources*, **242**, 314 (2013).
52. A. Tang, J. McCann, J. Bao, and M. Skyllas-Kazacos, *Journal of Power Sources*, **242**, 349 (2013).
53. J. T. Pukrushpan, A. G. Stefanopoulou, and H. Peng, *Proceedings of the American Control Conference IEEE*, **4**(12), 3117 (2002).
54. M. Bavarian, M. Soroush, I. G. Kevrekidis, and J. B. Benziger, *Industrial & Engineering Chemistry Research*, **49**(17), 7922 (2010).
55. D. A. McKay, W. T. Ott, and A. G. Stefanopoulou, *ASME 2005 International Mechanical Engineering Congress and Exposition*, Dynamic Systems and Control, Parts A and B, 1177 (2005).
56. D. A. McKay, J. B. Siegel, W. Ott, and A. G. Stefanopoulou, *Journal of Power Sources*, **178**(1), 207 (2008).
57. D. A. Knopf, B. P. Luo, U. K. Krieger, and T. Koop, *Journal of Physical Chemistry A*, **107**(21), 4322 (2003).
58. R. Carta, S. Palmas, A. M. Polcaro, and G. Tola, *Journal of Applied Electrochemistry*, **21**(9), 793 (1991).
59. Z. Wei, J. Zhao, M. Skyllas-Kazacos, and B. Xiong, *Journal of Power Sources*, **260**, 89 (2014).
60. F. M. White, *Fluid Mechanics*, McGraw-Hill, New York (2011).
61. C. N. Sun, K. L. More, G. M. Veith, and T. A. Zawodzinski, *Journal of the Electrochemical Society*, **160**(9), F1000 (2013).
62. H. Wu, X. Li, and P. Berg, *International Journal of Hydrogen Energy*, **32**(12), 2022 (2007).
63. H. A. Gasteiger, J. E. Panels, and S. G. Yan, *Journal of Power Sources*, **127**(1-2), 162 (2004).
64. E. A. Mason and A. P. Malinauskas, *Gas transport in porous media: The Dusty-Gas Model*, Elsevier, Amsterdam - Oxford - New York (1983).
65. A. Bertei and C. Nicolella, *Journal of Power Sources*, **279**, 133 (2015).
66. R. B. Bird, W. E. Stewart, and E. N. Lightfoot, *Fenomenos de transporte*, Reverte, Barcelona (1964).
67. J. H. Nam and M. Kaviany, *International Journal of Heat and Mass Transfer*, **46**(24), 4595 (2003).
68. R. C. Reid, J. M. Prausnitz, and T. K. Sherwood, *The Properties of Gases and Liquids*, McGraw-Hill, New York (1977).
69. J. O. Wilkes, *Fluid mechanics for chemical engineers*, Prentice Hall PTR (1999).
70. W. Xu, H. Zhang, F. Xing, H. Zhang, Y. Li, J. Cao, and X. Li, *Electrochimica Acta*, **118**, 51 (2014).
71. FuelCellStore, Properties of Nafion PFSA Membrane: 115, 117 and 1110.
72. V. Yu and D. Chen, *Journal of Solar Energy Engineering*, **136**(2), 021005-1 (2013).
73. G. Qiu, A. S. Joshi, C. R. Dennison, K. W. Knehr, E. C. Kumbur, and Y. Sun, *Electrochimica Acta*, **64**, 46 (2012).
74. Z. Tang, R. Svoboda, J. S. Lawton, D. S. Aaron, A. B. Papandrew, and T. A. Zawodzinski, *Journal of The Electrochemical Society*, **160**(9), F1040 (2013).
75. J. S. Newman and K. E. Thomas-Alyea, *Electrochemical Systems*, John Wiley & Sons, Inc., New York (2004).
76. A. J. Bard and L. R. Faulkner, *Electrochemical Methods: Fundamentals and applications*, John Wiley & Sons, Inc, New York (2001).
77. H. Hewa Dewage, Imperial College London (2016).
78. J. Golbert and D. R. Lewin, *Journal of Power Sources*, **135**(1–2), 135 (2004).
79. W. G. Bessler, *Solid State Ionics*, **176**(11–12), 997 (2005).
80. A. Bourke, M. A. Miller, R. P. Lynch, X. Gao, J. Landon, J. S. Wainright, R. F. Savinell, and D. N. Buckley, *Journal of The Electrochemical Society*, **163**(1), A5097 (2016).
81. E. Gileadi, *Electrode Kinetics for Chemists, Chemical Engineers and Materials Scientists*, John Wiley & Sons, Inc, New York (1993).